Modelling and analysis of crack turning on aeronautical structures

Llorenç Llopart Prieto

Modelling and analysis of crack turning on aeronautical structures

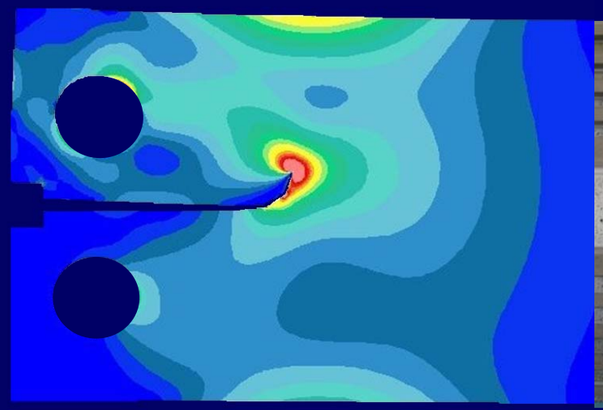

Doctoral Thesis

Llorenç Llopart Prieto

Director:
Dr. Marc Anglada i Gomila

Departament de Ciència dels Materials i Enginyeria Metal·lúrgica
UNIVERSITAT POLITÈCNICA DE CATALUNYA

Company director:
Elke Hombergsmeier

EADS
European Aeronautical Defence and Space company

EADS

UNIVERSITAT POLITÈCNICA DE CATALUNYA

UPC

EADS

Ottoburnn / Barcelona April 2007

6 Crack turning assessment

The analyses on crack turning predictions performed by means of the selected simulation program (StressCheck®) and experimental results of testing is treated in this chapter.

First section deals with the results and data collected at *TsAGI* (Central Aerodynamic Institute, Russia) from the testing of the *DCB*-specimens (set reference RU04). Here, the simulation used to analyse the connection between force, crack opening displacement and crack length is described. Performed crack path assessments are presented and compared with the experimental results of testing.

Section 6.2 deals with the influence of modelling details on the crack path predictions. The use of *3D*-models and the necessity to model notch geometry is discussed.

Third section describes the results obtained with the *DCB*-tests performed at *EADS* Corporate Research Centre (*CRC*) in Munich (set reference DE05) which were conceived on the basis of the attained results on the former section.

Sections 6.4 and 6.5 analyse respectively, the influence of the boundary on the crack path predictions and plastic behaviour, including the studies on crack-tip plasticity carried out by means of ARAMIS.

In section 6.6 crack path predictions based on the results obtained in the former sections are presented.

Finally, a conjunction of criteria is presented as a criterion. This is applied on the predictions of crack path for *DCB*- and *CFS*-specimens. The results are compared with the experimental results.

The *FE*-analyses in this chapter were carried out taking into account large deformations, i.e. with the geometric non-linear method. All geometric dimensions and mesh parameters of the modelled *DCB*- and *CFS*-specimens were created in parametric form. The dimensions of the *DCB/CFS*-models were those described in chapter 4; Figures 4.16 and 4.32 respectively. All regions were assigned with the elastic isotropic behaviour of the aluminium alloy *AA* 2024-T3

with the values in Table 4.5. First simulations were performed with polynomials with degrees from 5 to 8 in order to check the convergence of the solution and the quality of the mesh. The final results were evaluated from computations performed with polynomial of degree equal to 8.

6.1 Results from the test-set reference RU04

The experimental results on *DCB*-specimens with different notch lengths revealed distinct macroscopic fracture paths according whether crack propagation took place under cyclic or quasi static loading, as illustrated in Figure 6.1 (which assembles the main results of section 4.3.3).

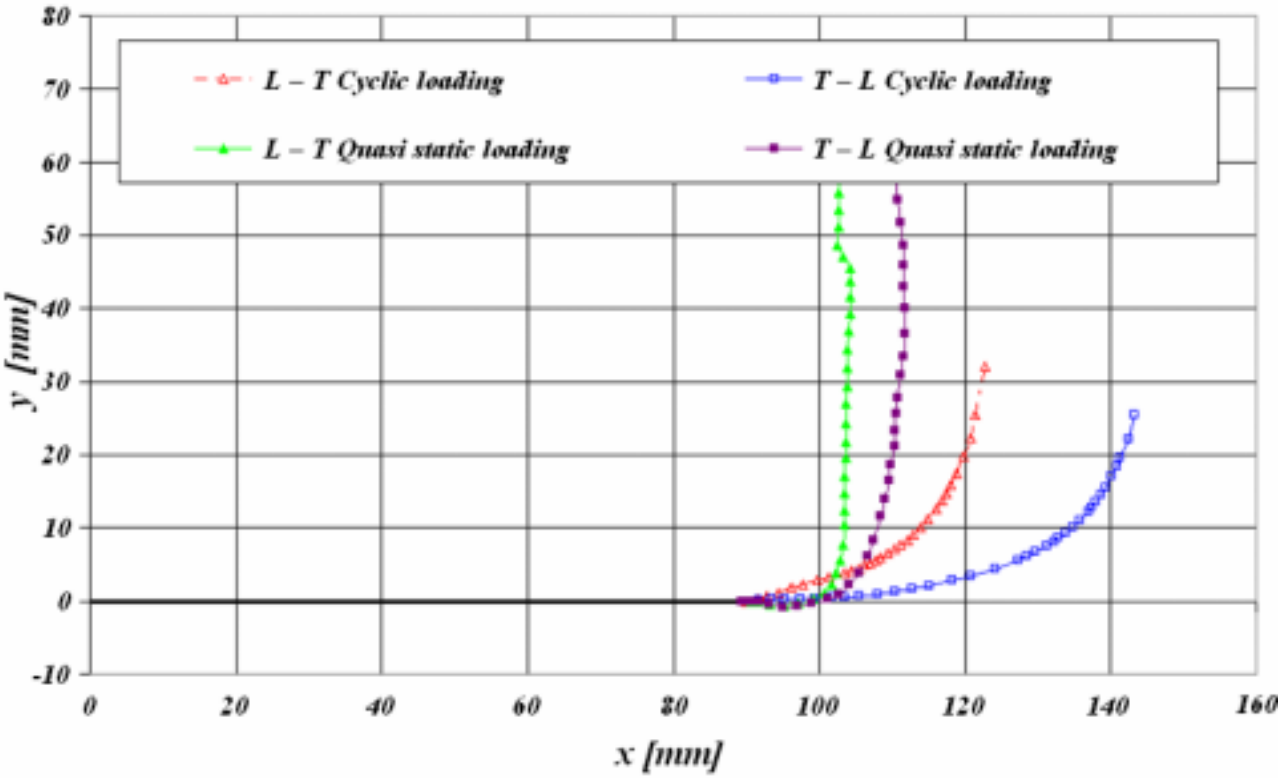

Figure 6.1. Representative results of crack path under cyclic and quasi-static loading for an initial notch length of 90 mm

It can be noticed that the turning angle is dependent on the anisotropy of the material and this is in agreement with literature results on the same type of specimens [9, 23, 69]. Furthermore, the following observations can be drawn from Figures 6.1 and 6.2:

a) under quasi-static and cyclic loading the crack turns more sharply in L-T than in T-L specimens.

b) the crack turning angles under quasi-static loading are larger than under cyclic loading.

c) under quasi-static load the crack turns more sharply with longer notch lengths

d) it seems to be a saturation notch length above which the start for crack turning is not anymore influenced by the anisotropy of the material, i.e. with longer notch lengths the crack path in T-L and L-T specimens tends to be similar (as represented in Figure 6.2).

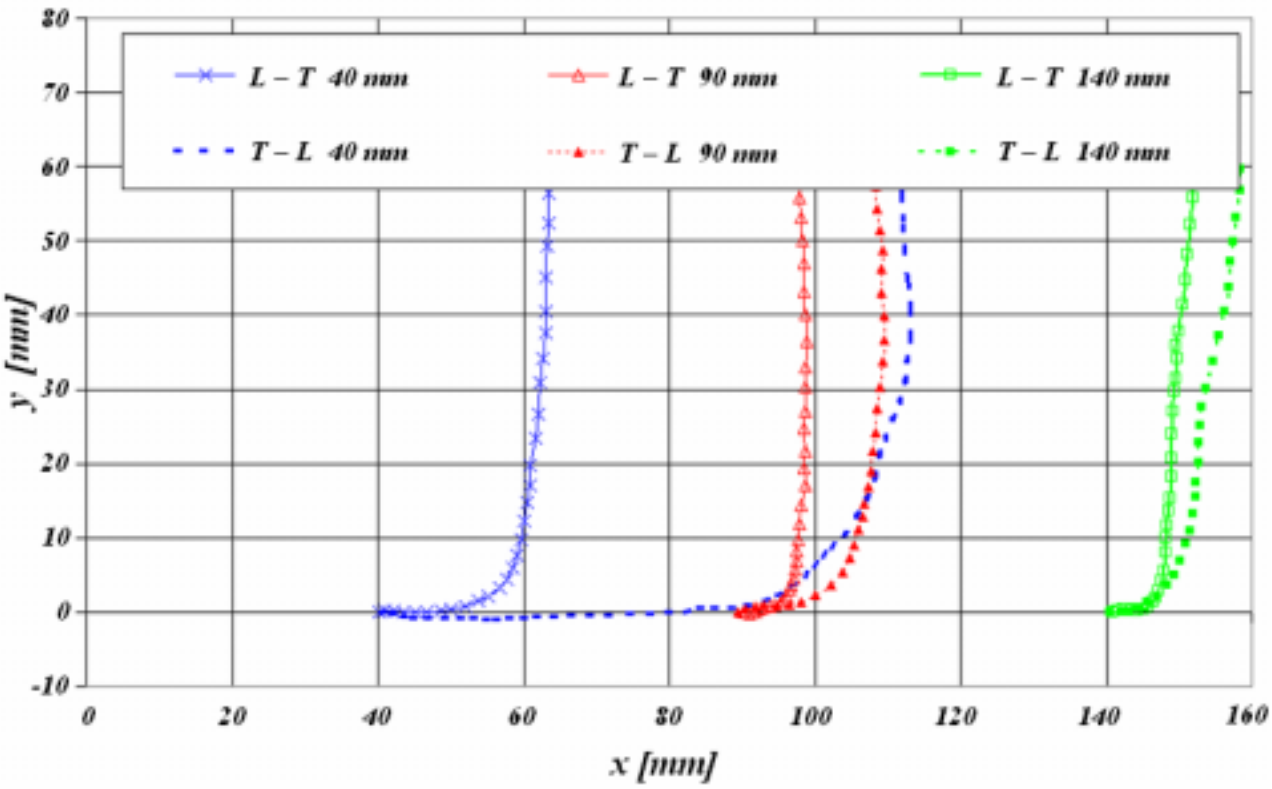

Figure 6.2. Representative results of crack path under quasi-static loading for an initial notch length of 40, 90 and 140 mm in L-T and T-L

e) Cracks tend to be attracted by boundaries and they are increasingly stable as a boundary is approached.

Another important observation was that under both load conditions, there was a transition of the orientation of the surfaces of the crack plane from 0º to 45º, i.e. the crack surface turned with reference to the thickness direction, ψ. This phenomenon took place before the crack turning event.

6.1.1 COD-F-Crack length

In order to be able to simulate the crack propagation under quasi-static load using *LEFM*, it is necessary to know the degree of plasticity in the specimen at each crack length. This is directly related to the actual applied force for each position of the crack tip, and therefore the correspondence between a_i and F_i is needed. Furthermore, crack turning predictions are dependent on K_{II}/K_I- or/and K_I/T-ratios, which, in turn, are determined by the applied force on specimens suffering large deformation. However, only the connection between the force and the crack opening displacement was recorded because it was assumed that large displacements do no influence the crack path. For this reason, *FE*-analyses were performed in order to obtain this information.

To this aim, three groups of *FE*-models of the *DCB*-specimen were generated with StressCheck® in *2D*, that is, one for each notch length (*40*, *90* and *140* mm). The crack paths used in these models were those obtained on the experimental results of testing. The upper and bottom nodes at the end of the specimen were fixed in the *y*- and the *z*-directions and the middle node at the end of the specimen was fixed in the *x*-direction. Figure 6.3 presents the mesh and the described boundary conditions.

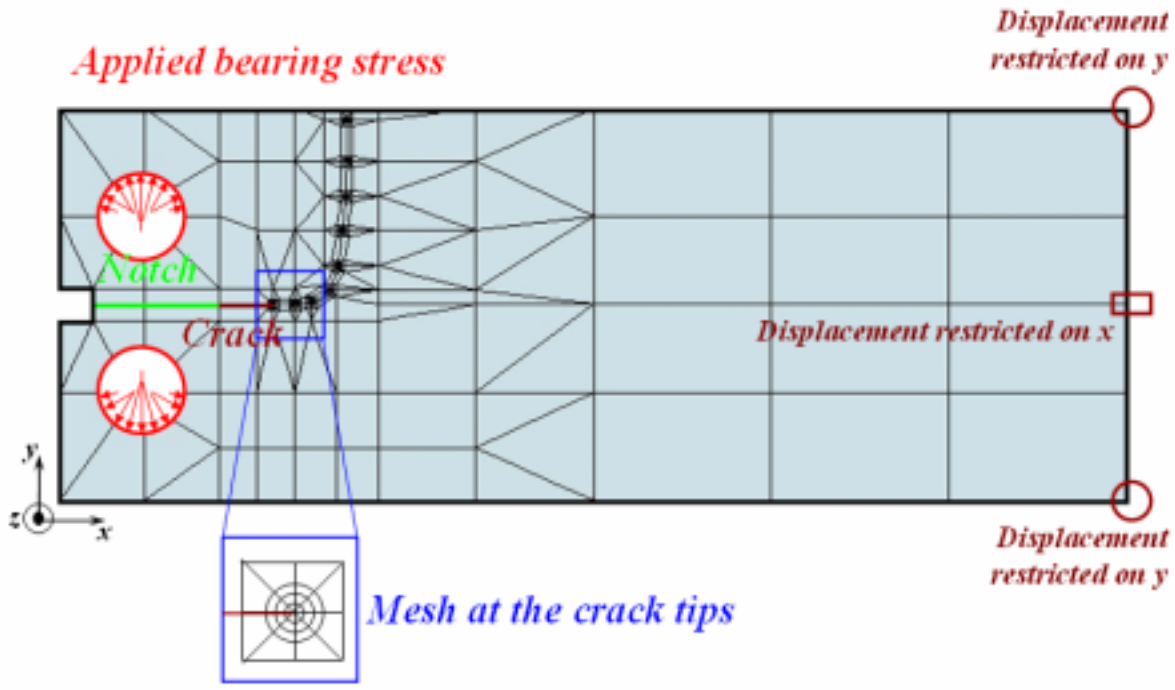

Figure 6.3. DCB-model with 40 mm notch with the crack path from test results of reference RU04

The number of elements was between 350 and 400 depending on the model group. Every modelling group was formed by six quasi-identical models differentiated on the position of the crack tip. Each crack tip coordinates (i.e. *x* and *y* on the specimen) correspond to different positions on the experimental crack path. For example, Figure 6.4 and Table 6.1 show the six selected crack tips for the analyses of the *40* mm notched models.

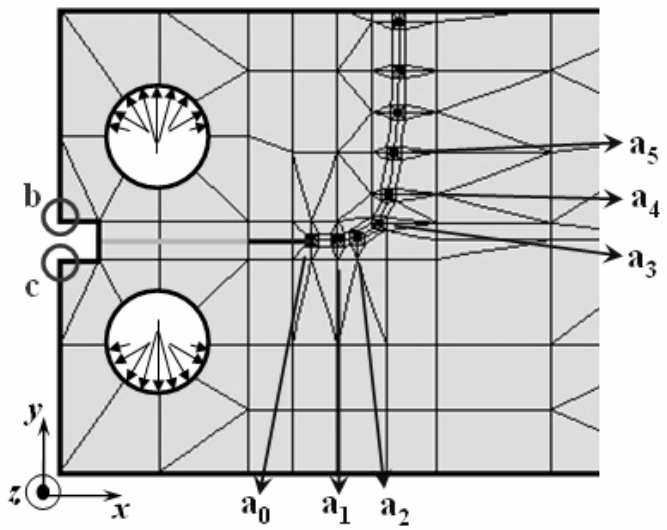

Figure 6.4. Selected crack path coordinates

Table 6.1. Coordinates of the selected crack path to be analysed by means of simulation

Selected points	*Coordinates*	
	x [mm]	*y [mm]*
a_0 *(40 mm notch)*	40.0	0.0
a_1	46.8	0.1
a_2	52.0	0.8
a_3	57.7	4.5
a_4	60.2	12.2
a_5	61.6	23.4

Three different forces from *0.5* to *11 kN* were applied in the form of bearing stresses at the upper and lower holes of the specimen for the defined crack lengths (a_0, a_1, a_2, a_3, a_4 and a_5). On the post processing, the values of the *COD* at the mouth of the notch, points *b* and *c* in Figure 6.4, were plotted for every force and crack length in a diagram containing the experimental values of force vs. *COD*, which is depicted in Figure 6.5 for the *40* mm notched specimen.

Table 6.2. Correlation between crack tip position, COD and force for the DCB with a 40 mm notch

Selected points	*Coordinates*		*COD*	*F*
	x [mm]	*y [mm]*	*[mm]*	*[kN]*
a_0 *(40 mm notch)*	40.0	0.0	1.46	6.510
a_1	46.8	0.1	2.73	9.452
a_2	52.0	0.8	3.61	10.169
a_3	57.7	4.5	4.44	10.020
a_4	60.2	12.2	5.13	9.129
a_5	61.6	23.4	-	-

The intersections of the simulated curves with the experimental test curve determined the highest force that each crack tip position sustained before propagation. From these intersections the

connection between force-crack length and *COD* were determined as summarised in Table 6.2 for the *40* mm notched specimen.

By following this, all the *F-COD*-crack length relationships were determined.

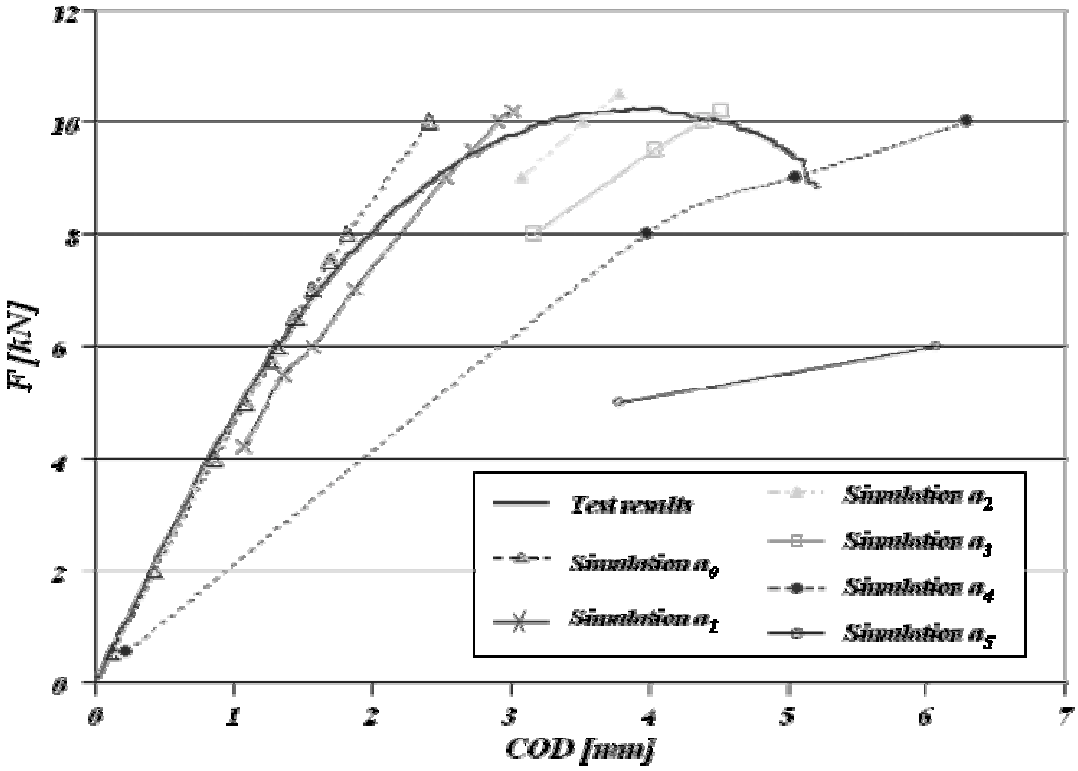

Figure 6.5. Test and simulation results of the DCB with a 40 mm notch. F-COD-a relation

6.1.2 Crack path prediction on DCB-specimens

Crack turning criteria was evaluated comparing simulated crack paths with those from the experimental results of testing (ref. RU04). To this aim, two different modus operandi can be used. The first one consists on modelling merely crack tip positions corresponding to the path obtained on the test results, e.g. a_1 to a_5 in Figure 6.4. Afterwards, fracture parameters are computed on each crack tip and these parameters are used in turning criteria to calculate the turning angles. Finally, the predictions of the turning angle can be compared with those from test results.

The second possibility lies in predicting a complete crack path for each turning criteria. The predicted paths are then compared with experimental results. This kind of analysis implies an

iterative process. First a *DCB*-specimen is modelled with its correspondent notch length. The fracture parameters K_I, K_{II} and *T*-stress are computed. After that, the turning angle is calculated using the selected turning criterion and the crack is incremented on the model in the calculated direction. This process is carried out repeatedly until a predefined crack length or the end of the specimen is reached, or until *LEFM* loses its validity.

The use of the first approach will not result in comparable outcomes since experimental results of testing show deviations on crack paths in specimens of the same group, i.e. same length of the notch, same specimen direction and same load as shown, for example, with the green or red crack paths in Figure 6.6. This means that different relative turning angles are possible and consequently no comparison is feasible. For this reason, the second approach was used.

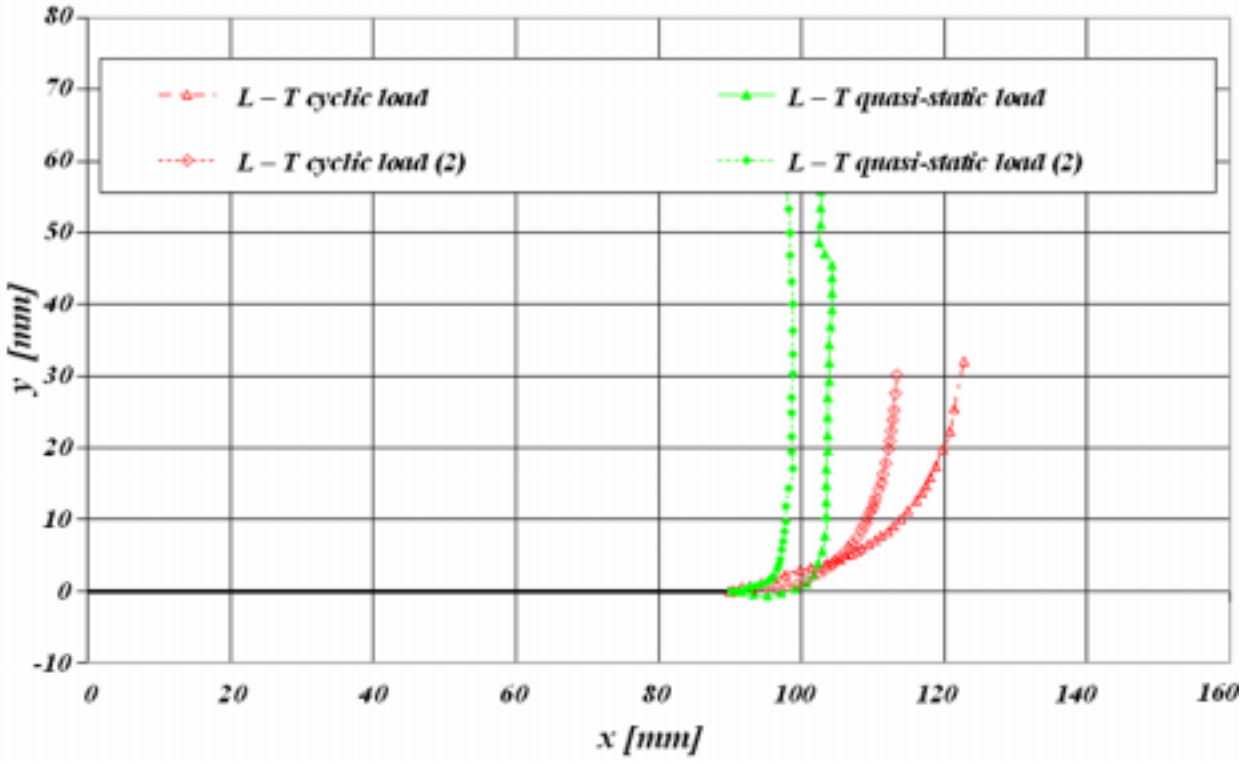

Figure 6.6. Crack paths for the DCB-specimen in L-T direction with a notch length of 90 mm

The *FE*-analyses performed in this section were in line with the analyses described in Chapter 5. The *DCB*-specimens were modelled in *2D* with a *40* mm notch. The upper and bottom nodes at the end of the specimen were fixed in the *y*- and the *z*-directions and the middle node, at the end of the specimen, was fixed in the *x*-direction. The mesh and the boundary conditions were a mixture between those used in the models defined in Figures 5.15 and 6.3. The number of

elements increased during crack propagation from 90 until 300. An absolute crack increment of *5* mm was applied.

For each model, a traction force was applied in the form of a bearing stress at the upper and lower holes of the specimen. This force was varied between *4588* and *10138* N according to the results obtained in section 6.1.1.

Figure 6.7 illustrates the predicted crack path using the described models. The extracted fracture mechanics parameters and the calculation of every crack turning angle for each crack length are given in Table 6.3 for the criterion developed by Finnie & Saith, Kosai, Kobayashi & Ramulu and Shiamoto et al. (in this work called *WEF*-criterion) with a r_c value of *3* mm.

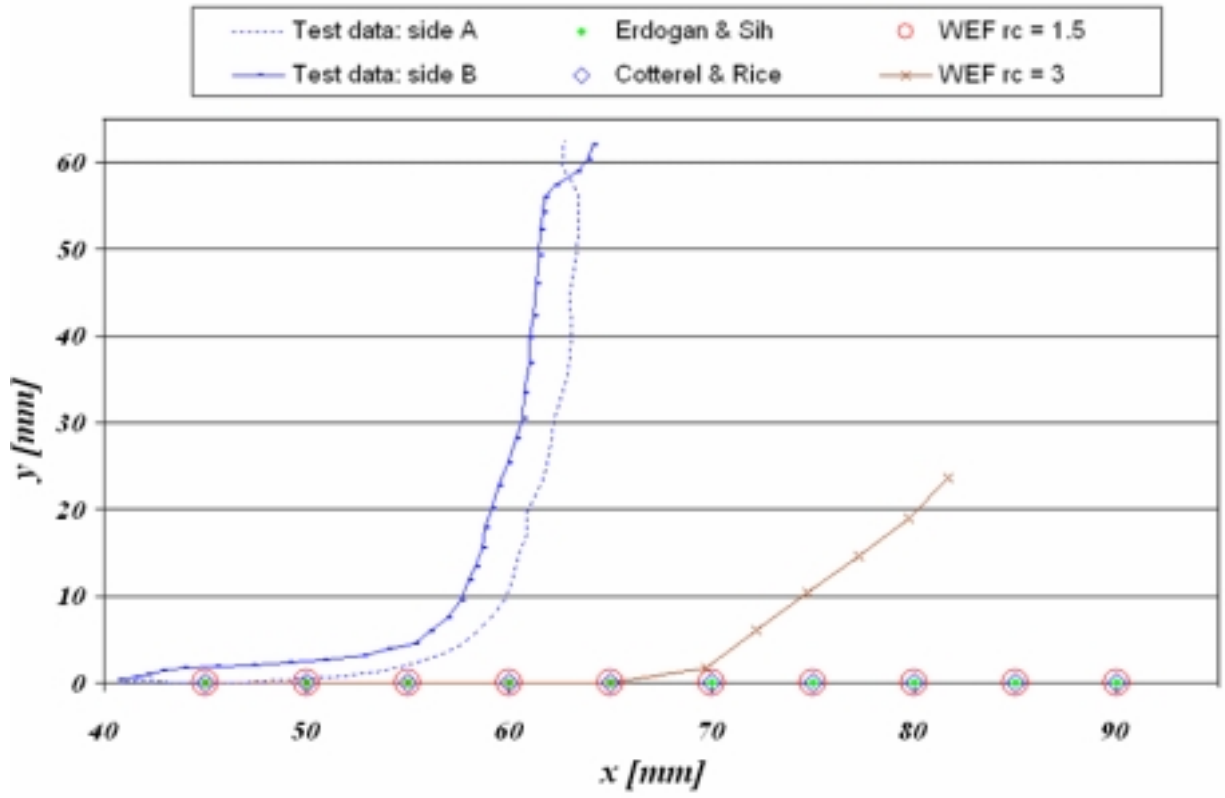

Figure 6.7. Crack path predictions using a 2D-model with 40 mm notch under quasi-static loading

It has to be remarked that the turning angles, φ_c, calculated from crack turning criteria, correspond to the turning from the actual crack orientation, i.e. it is a relative angle. The absolute angle refers to the global coordinate system. Figure 6.8 depicts the definitions of relative and absolute turning angle. In this case φ_i corresponds to both a relative and absolute angle.

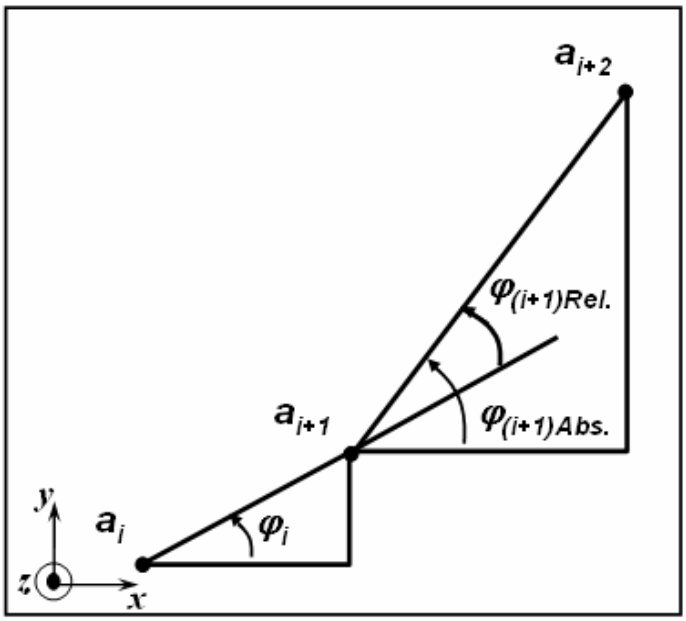

Figure 6.8. Definition of the relative (Rel.) and absolute (Abs.) turning angle

Table 6.3. Crack path calculations with the WEF-criterion with r_c = 3 mm

Δa [mm]=5								***Absolute angle***	***r_c = 3 mm***	
Notch	***x [mm]***	***y [mm]***	***K_I [MPa*m$^{1/2}$]***	***K_{II} [MPa*m$^{1/2}$]***	***T [MPa]***	***F [N]***	***φ_c [°]***		***r_0 [mm]***	***$r_c > r_0$***
a_0	40.0	62.0	41.6	-1.9x10^{-6}	78.8	4588	0.0	0.0	6.228	False
a_0+Δa	45.0	62.0	70.8	-3.2 x10^{-6}	149.6	7319	0.0	0.0	5.009	False
a_0+2Δa	50.0	62.0	92.2	-3.6 x10^{-6}	214.4	8986	0.0	0.0	4.140	False
a_0+3Δa	55.0	62.0	105.0	-4.3 x10^{-6}	264.8	9687	0.0	0.0	3.520	False
a_0+4Δa	60.0	62.0	114.0	-4.5 x10^{-6}	307.8	9991	0.0	0.0	3.070	False
a_0+5Δa	65.0	62.0	121.4	-4.5 x10^{-6}	347.3	10138	-19.8	19.8	2.736	True
a_0+6Δa	69.7	63.7	125.3	9.0	358.7	10113	-40.4	59.9	2.731	True
a_0+7Δa	72.2	68.0	115.8	25.0	261.3	9625	-44.0	103.9	4.393	False
a_0+8Δa	74.7	72.3	125.8	17.0	213.1	8990	-29.6	89.5	7.795	False
a_0+9Δa	77.2	76.7	135.8	10.6	202.1	8353	-17.8	77.7	10.099	False
a_0+10Δa	79.8	81.0	147.0	4.8	205.5	7714	-7.5	67.4	11.450	False

As can be observed in Figure 6.7 and Table 6.3 the predictions of crack tuning by means of the used model and different criteria does not deliver reliable crack paths.

For this reason, a deep analysis was necessary to find out the cause. One explanation could be the simplification of the modelled specimen. It seems, according to [6] that the notch has an important influence on the crack turning and, consequently, it should be modelled with an opening gap, i.e. lack of material.

6.2 Modelling influences on crack path predictions

This section evaluates the effect of three dimensional modelling and modelling details, as the notch geometry, on crack path predictions.

6.2.1 3D-effects

Three dimensional analyses show that *Mode III* loading conditions are created along the crack front although the external loading does not contain an out-of-plane shear component [95]. *Mode III* is related to a mode coupling effect caused by Poisson's ratio and the laterally relaxed constraints adjacent to the free surfaces of the specimen. Due to this effect, as well as to the differences between plane stress and plane strain, a curved crack tip is formed.

The importance of modelling the form of the crack front must be cleared before dealing with crack turning assessment. First part of this section evaluates the necessity of a detailed crack front comparing simulation results of curved and straight crack fronts on the *2SP*-specimen. Second part analyses the influence of the observed crack front twisting, angle ψ, based on *DCB*-specimens.

Based on the fracture surfaces of the *2SP*-structure (set reference DE03), represented in Figure 6.9.a, a curved crack front was introduced to the model as depicted in Figure 6.9.b. The modelling conditions were exactly the same as described in section 5.3.3 and represented in Figure 5.7.b.

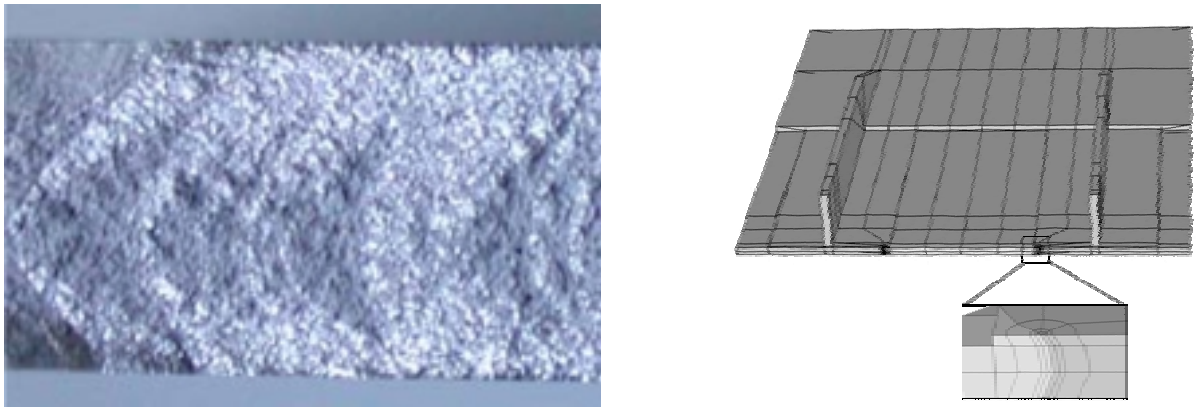

a) ***b)***

Figure 6.9. a) Fracture surface of the 2SP-specimen and b) 2SP-model with the crack front on a)

The growth of the crack front was simulated by propagating first the point with the highest stress intensity factor along the crack front with the user defined extension, Δa.

For the curved crack, the amount of crack growth at any point, Δa_i, was based on the ratio SIF/SIF_{max}, i.e. $\Delta a_i = \Delta a\ (SIF/SIF_{max})$. For the straight crack front the existent inclination was remodelled at the new position defined by the growth applied at the point of the crack front with highest *SIF*.

The results obtained with this modelled structure (detailed model) were compared with those obtained for a straight crack front (simplified model) and depicted in Figure 6.10.

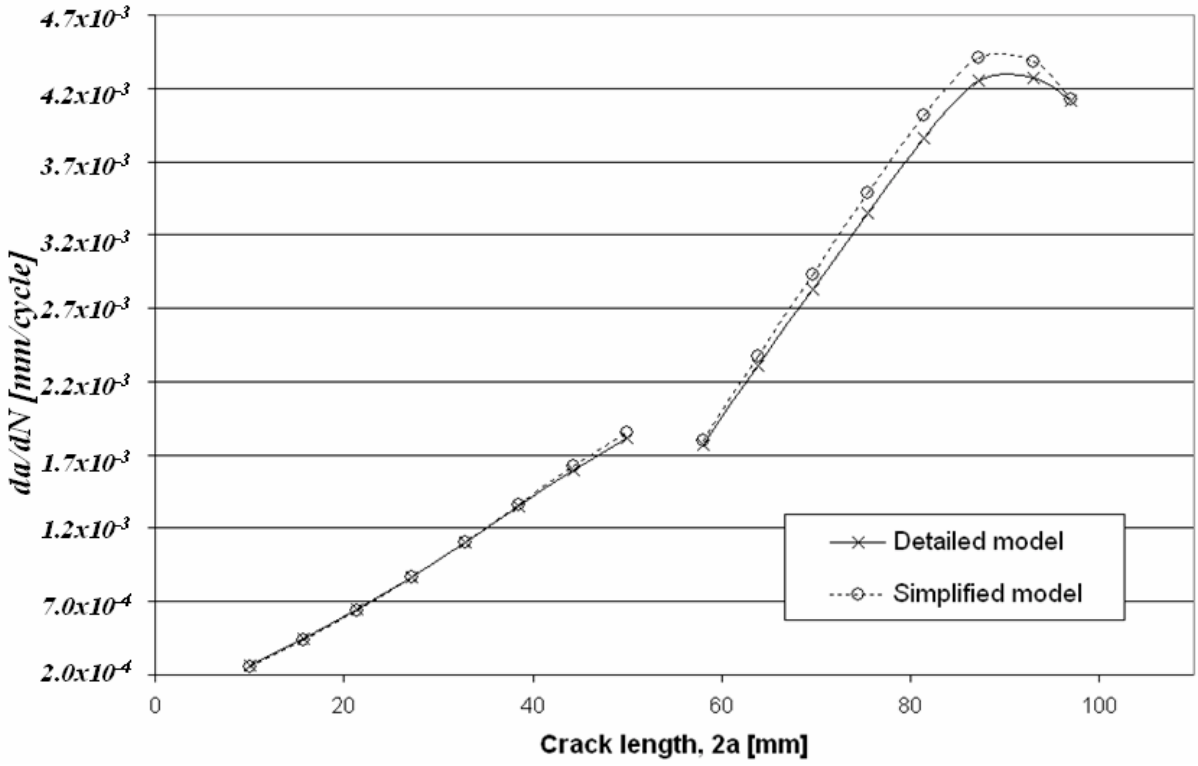

Figure 6.10. Simulation results with straight crack front and curved crack front model [82]

Based on these results it can be concluded that the modelling of a curved or straight crack front does not influence the crack growth prediction. According to this result, the modelling of a *3D*-crack front was represented, from now on, as a straight line. Besides, this will reduce the time for the creation of the model and computation time.

Analysing more in detail the crack path on the *DCB*-test, it was observed that the crack surfaces experimented a rotation on the plane *xz*, i.e. with an angle ψ. The coordinate *x* is defined in the direction parallel to the notch length and perpendicular to the direction of the applied force and *z* is in the thickness direction as represented in Figure 6.3. This inclination of the crack remained constant along the crack path until failure.

With the purpose of analysing the effect of this crack inclination on crack path predictions, full *3D DCB*-models were generated with *StressCheck*®. The upper and bottom nodes at the end of the specimen were fixed in the *y*- and the *z*-directions and the middle nodes at the end of the specimen were fixed in the *x*-direction. The number of elements changed from 200 to 350 depending on the crack propagation step. Because the configuration of the inclined crack front was not known, three different configurations of the crack front were assumed and modelled based on the inputs from the experimental results of testing set ref. RU04. These were created after measuring the crack paths on both sides of the *DCB*-specimens. The measured data was delivered under a tabular form for both sides (A and B) as represented in Table 6.4.

The modelled crack fronts are represented in Figure 6.11.

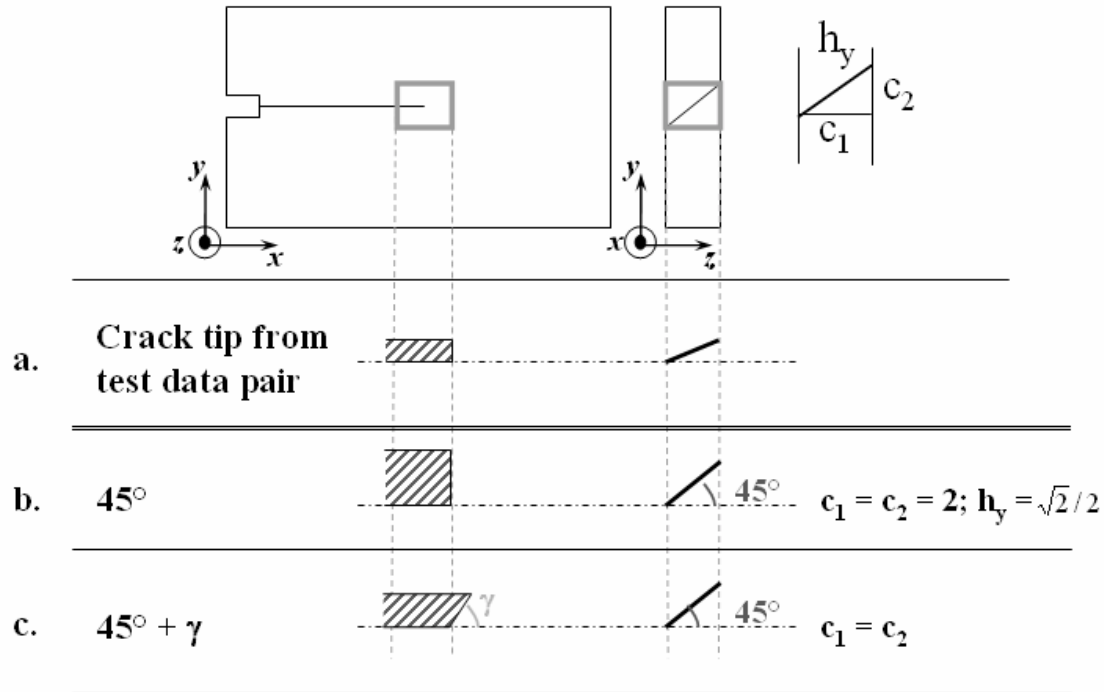

Figure 6.11. Modelled 3D crack fronts

Table 6.4. Received crack path data for a notch length of 90 mm in L-T under cyclic loading. Ref. RU04

Side A		***Side B***	
x [mm]	***y [mm]***	***x [mm]***	***y [mm]***
0	0	0	0
90.328	0	90.328	0
91.768	0.296	91.711	-0.487
93.525	0.402	93.151	-0.487
95.050	0.445	94.718	-0.381
96.532	0.551	95.904	-0.296
97.930	0.699	97.683	0.212
99.370	0.995	99.059	0.826
100.810	1.567	100.372	1.461
102.419	2.393	102.108	2.245
103.054	2.795	102.786	2.689
103.584	3.219	103.315	3.049
104.261	3.706	103.929	3.473
104.791	4.193	104.543	4.023
105.489	4.828	105.158	4.531
106.019	5.315	105.729	5.124
106.612	5.993	106.428	5.781
107.120	6.649	106.979	6.416
107.776	7.602	107.593	7.242
108.369	8.555	108.101	8.110
108.708	9.105	108.588	8.830
108.941	9.571	108.906	9.423
109.301	10.249	109.160	9.995
109.619	10.948	109.498	10.630
109.957	11.604	109.837	11.477
110.212	12.388	110.113	12.239
110.423	13.065	110.409	13.065
110.826	14.103	110.663	13.743
111.164	15.183	111.044	15.056
111.461	16.368	111.341	16.093
111.821	17.914	111.701	17.787
112.160	19.778	112.082	19.291
112.329	20.921	112.378	20.582
112.604	22.276	112.527	21.768
112.753	23.949	112.865	23.928
112.922	25.241	113.077	24.817
113.2184	27.63372	113.183	27.46412
113.2819	30.17475	113.2889	29.85693

The assumed crack front in case **a** (crack tip from test data pair) was defined with the tabular data taking the coordinates on both sides of the specimens with similar *x*-values. For example, if side A is defined with the coordinates (*x=91.768, y=0.296*), side B will be (*x=91.711, y=-0.487*) as this corresponds to the data pair with *x* around *91.7*. The crack front is then the line connecting these two points.

The crack front for case **b** (*45*º) was defined by the line that connects two points on the specimen surfaces with exactly the same *x*-value and differing on one specimen thickness, *t*. This defined c_1 and c_2 in Figure 6.11 to be equal to *t*, and so, assuring the smaller crack front with a 45º inclination. Thus, if one surface point has coordinates (x_1, y_1), the second surface point situated on the opposite side of the specimen has coordinates (x_1, y_1+t) or (x_1, y_1-t).

The third crack front, case **c** (defined as $45º + \gamma$) used again the experimental crack paths, and assumed that the inclination of the crack front, ψ, was exactly *45*º. With these two conditions, i.e. *45*º and crack path data, the coordinates of the points at the intersection between the crack front and the surfaces of the specimen were determined. This can produce the selection of two points with different *x*- and *y*-values.

The fracture parameters were calculated on three representative points of these modelled crack fronts. One corresponded to the middle of the specimen which was characterised by plane strain conditions. The other points were selected to be near the specimen surfaces, which are under plane stress. However, these last points could not lie on the specimen surface because it has to be assured that the integration contour, Γ, is contained in the specimen as represented in Figure 6.12. It has to be remembered that the fracture parameters are computed based on the *J*-integral, and the contour of integration is defined perpendicular to the crack front.

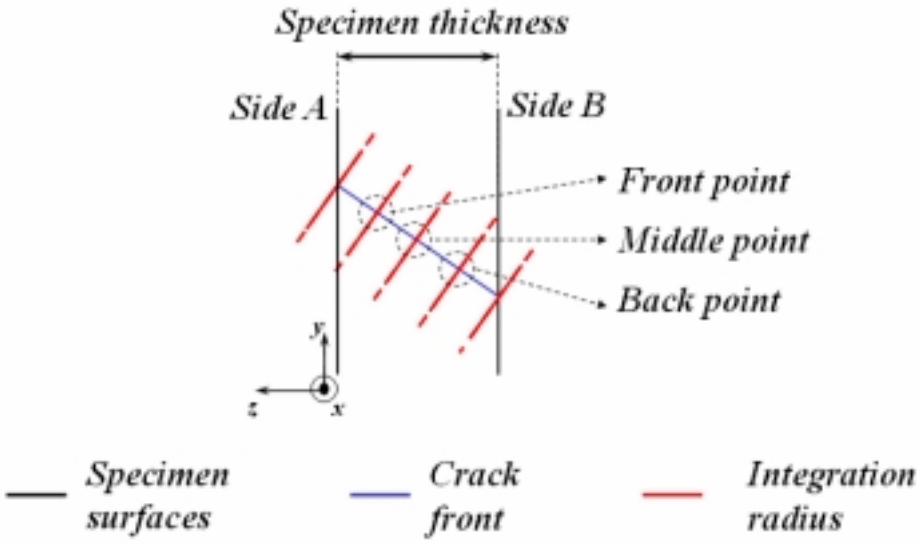

Figure 6.12. Definition of the locations at the crack front, where the fracture parameters were calculated

Crack path predictions were performed taking into account only the extracted fracture parameters at back, middle or at the front points by means of both the Erdogan & Sih and the *WEF*-criterion.

The results showed the same crack path for the three modelled crack fronts and with the calculated fracture parameters at the middle, back and front points. Figure 6.13 summarises the predicted crack paths.

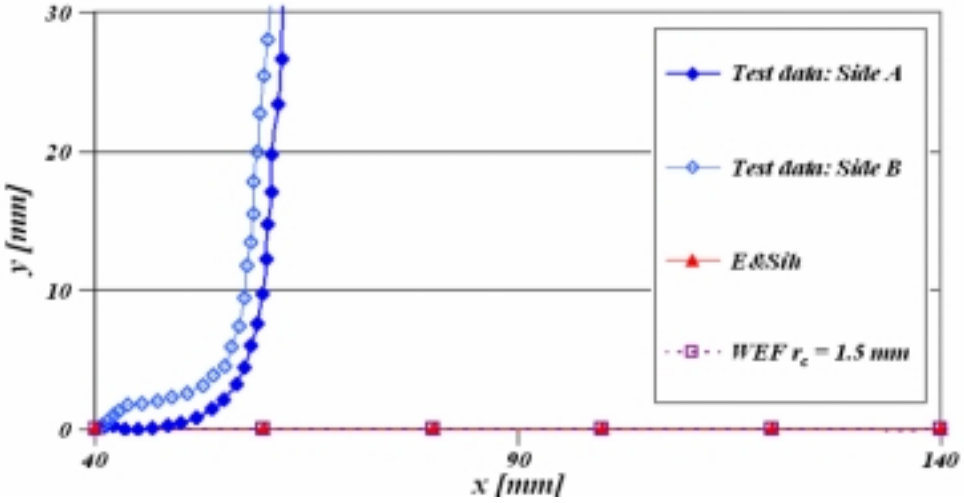

Figure 6.13. Crack paths predicted for different crack fronts and analysed points

As can be observed in Figure 6.13 the predictions of the *3D*-models with different crack front inclinations deliver no crack turning and therefore, it was concluded that the crack inclinations on ψ do not affect the predictions of crack paths for *DCB*-specimens.

6.2.2 Notch geometry and Modelling details

According to [95] the meshing algorithm requires a finite initial crack-opening gap, which has been observed to adversely affect *T*-stress. Because second order criteria are dependent on this stress, the opening gap and, consequently, notch geometry could have an important influence on the crack path, specially, on the initiation of the crack turning. Furthermore, this gap can promote the generation of *Mode II* [95].

DCB- and *CFS*-specimens were used to analyse this phenomenon by means of simulation. The automatic crack propagation capability of StressCheck® was employed. This requires two

dimensional geometry constructions containing simple closed loops. Additionally, every boundary condition and constraint must be defined as a set associated with a unique *ID*. A set is here a collection of objects (points, boundaries, nodes, elements etc.). The automatic crack propagation accomplished under the defined conditions by automeshing the solid model with the crack, computing the principal stresses, evaluating the new crack direction (based on the maximum stress criterion), deleting the generated mesh, and finally, propagating the crack on the new computed direction. This process was applied iteratively until the maximum crack length or the pre-defined number of iterations was reached. For more information about this capability of StressCheck® reference [96] can be consulted.

Attending the above defined conditions, different solid representations of the *DCB* and the *CFS* were generated in *2D*.

The models of the *DCB*-specimens represented the specimen with a notch length of *40* mm. Four different sets were created in form of boxes surrounding the limits, where constrains and boundary conditions had to be applied. Two sets defined the upper and bottom areas at the end of the specimen to fix the specimen in the *y*-direction. Another set was located at the middle-end of the specimen to fix the specimen in the *x*-direction. The last two sets were placed around the two clamping circles to apply a load of *100* MPa in the form of a bearing stress. Figure 6.14 illustrates the created *DCB*-solid model and locates the five used sets/boxes.

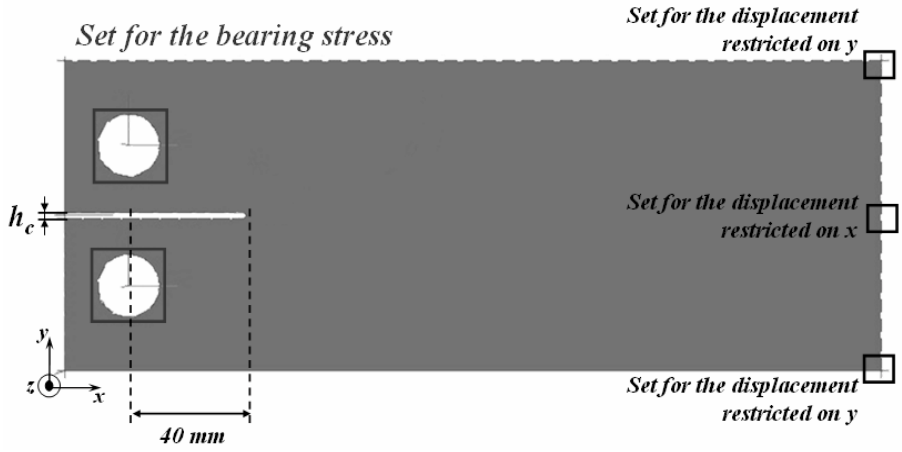

Figure 6.14. DCB-solid model and sets definition

Two different crack tip geometries, round and quadratic, were modelled. The *DCB*-models with the quadratic notch were analysed with a pre-crack length, *d*, equal to *1*, *3*, *5* and *7* mm at the corner of the notch and with *d = 1* at the middle of the notch. Two different gap openings of the

notch, h_c, equal to *1* and *0.3* mm were analysed for the quadratic notch. All pre-defined notch and notch + pre-crack lengths were equal to *40* mm. Figure 6.15 illustrates the modelled notches and the two described pre-crack positions.

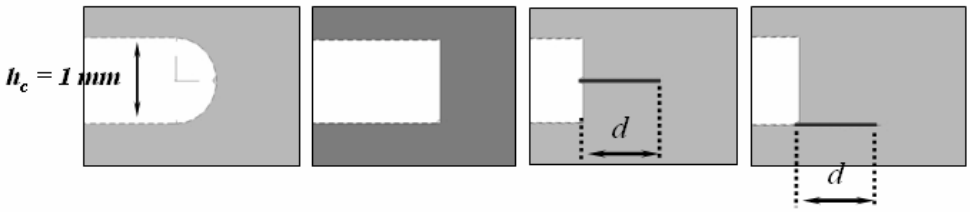

Figure 6.15. Crack tip geometries and pre-crack positions

Four *CFS*-models were generated with StressCheck® in *2D*. Figure 6.16 illustrates the models that take profit from the symmetry axis and consequently only the half of the *150* mm notch length was introduced, i.e. *75* mm.

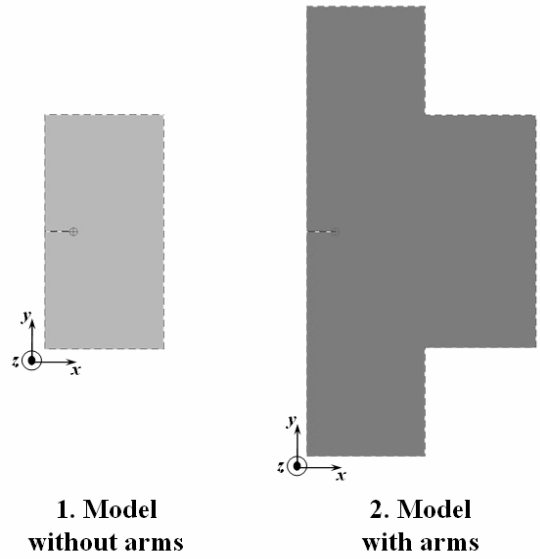

Figure 6.16. Simplified CFS-models

The reason of the arms on the *CFS*-specimen is to eliminate clamping influences on crack growth. The grooves were machined in order to assure the introduction of pure tension, otherwise the Poisson effect would introduce shear stresses.

Because *FE*-modelling allows the introduction of load directly at the boundaries, no effects due to clamping device exists and therefore the first model was created without arms.

Four different sets were created in form of boxes surrounding the limit, where constrains and boundary conditions have to be applied for the above models. One box was placed vertical at the left side of the models defining the line for symmetry condition. Two other boxes were defined for the upper and bottom lines to apply a normal tension of *75.32* MPa perpendicularly to the crack and to restrict the movement in the *x*-direction. The last box was defined at the right line of the models to apply a normal tension of *107.6* MPa parallel to the crack and to restrict the movement in the *y*-direction.

Figures 6.17 and 6.18 sketch the created full models of the *CFS*-specimen with a notch length of *150* mm. The differences between *4a*, *4b* and *4c* lay on the complexity of the model which included fillet and grooves details.

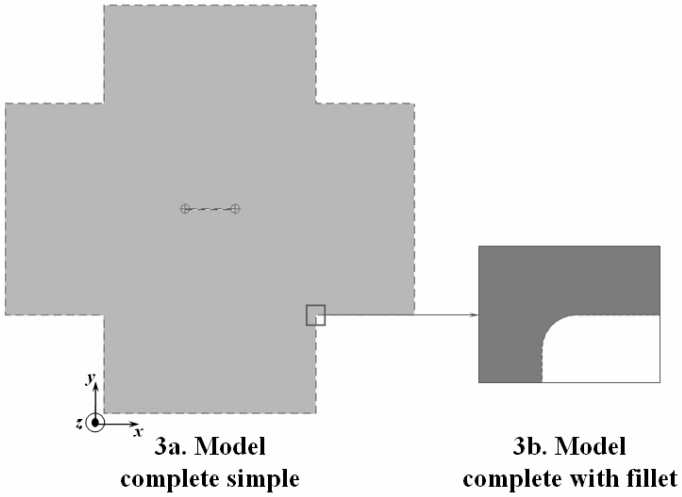

Figure 6.17. Full CFS-models without grooves

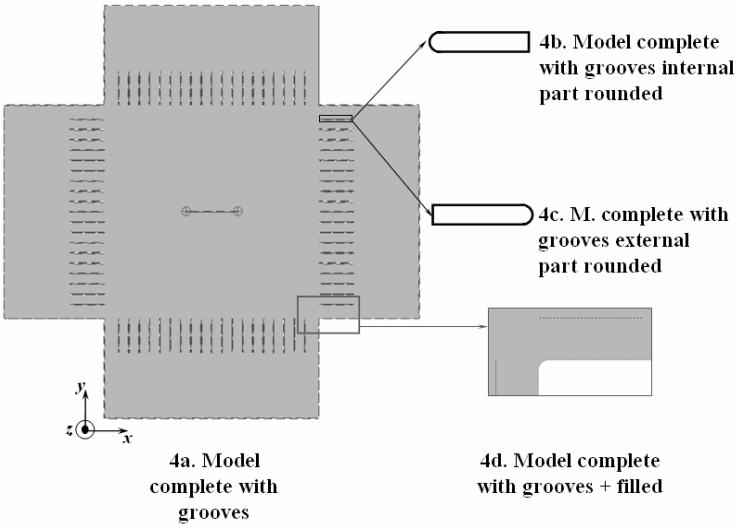

Figure 6.18. Full CFS-models with grooves

For each *CFS*-model, five different crack or notch geometries were generated, that is, one with no gap and four with gap opening of the notch. The values of the gap opening (notch thickness) were *2*, *1*, *0.2* and *0.02* mm.

An example with the computed crack path is depicted in Figure 6.19 for the *DCB* with the rounded notch-tip and the last generated mesh.

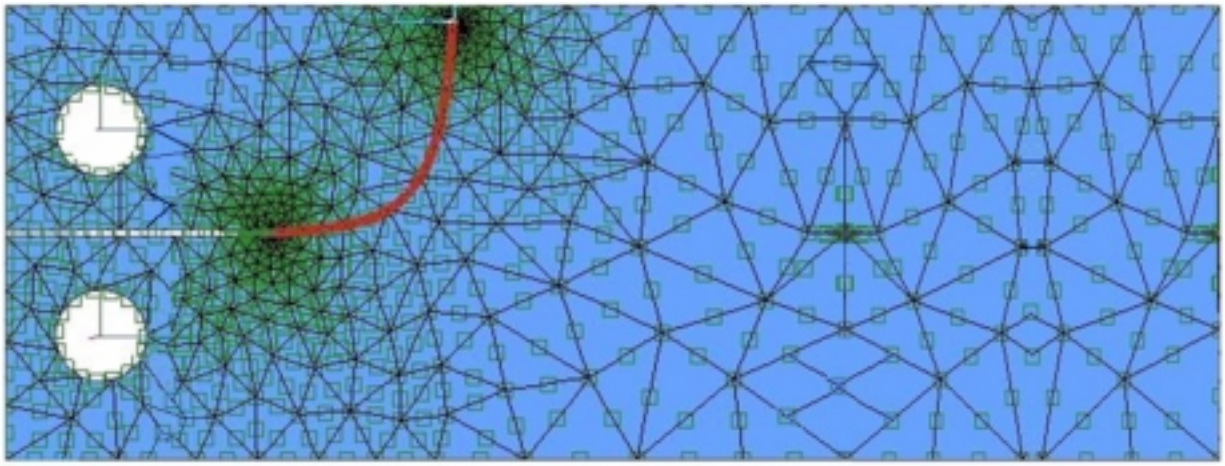

Figure 6.19. Automatic crack path for the model with the rounded notch

The number of elements created ranged between 420 and 860 for the *DCB* and 700 and 2000 for the *CFS*-models. These were dependent on the model, the notch, the pre-crack and the crack propagation step.

A pre-analysis on the *DCB* was launched with three different crack increments, Δa, of *1*, *5* and *7* mm for the quadratic notch model. A number of 20 iterations were introduced and the maximal crack length was set to *100* mm. A polynomial order of 4, 6 and 8 was used for the round notch analyses.

In Figures 6.20 and 6.21 it is plotted the predicted crack path in terms of the defined crack increment and polynomial order, respectively. As can be observed, there is no much influence on the predicted crack path due to different crack increments and there is no effect for different polynomial orders. Lower polynomial order generated convergent results because the mesh created during the crack path analysis was quite dense.

However, the time of the simulation was significantly increased with smaller Δa and higher polynomial order. Therefore, for the further analyses on the *DCB*- and the *CFS*-models a polynomial order of 4 and a crack increment equal to 5 mm were used.

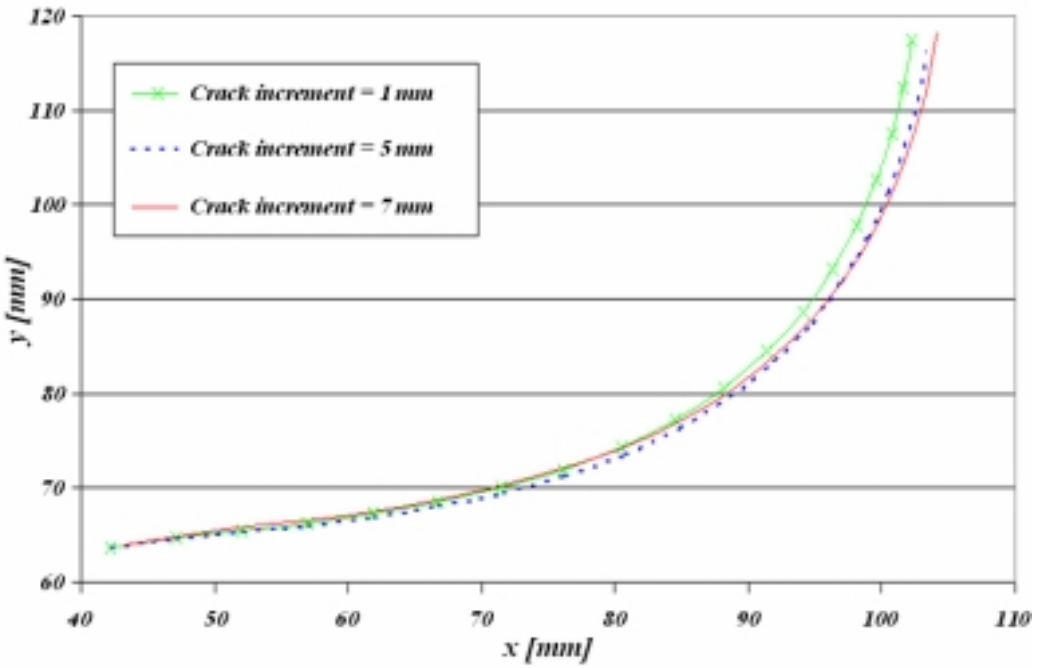

Figure 6.20. Crack path results for different crack increments (quadratic notch model)

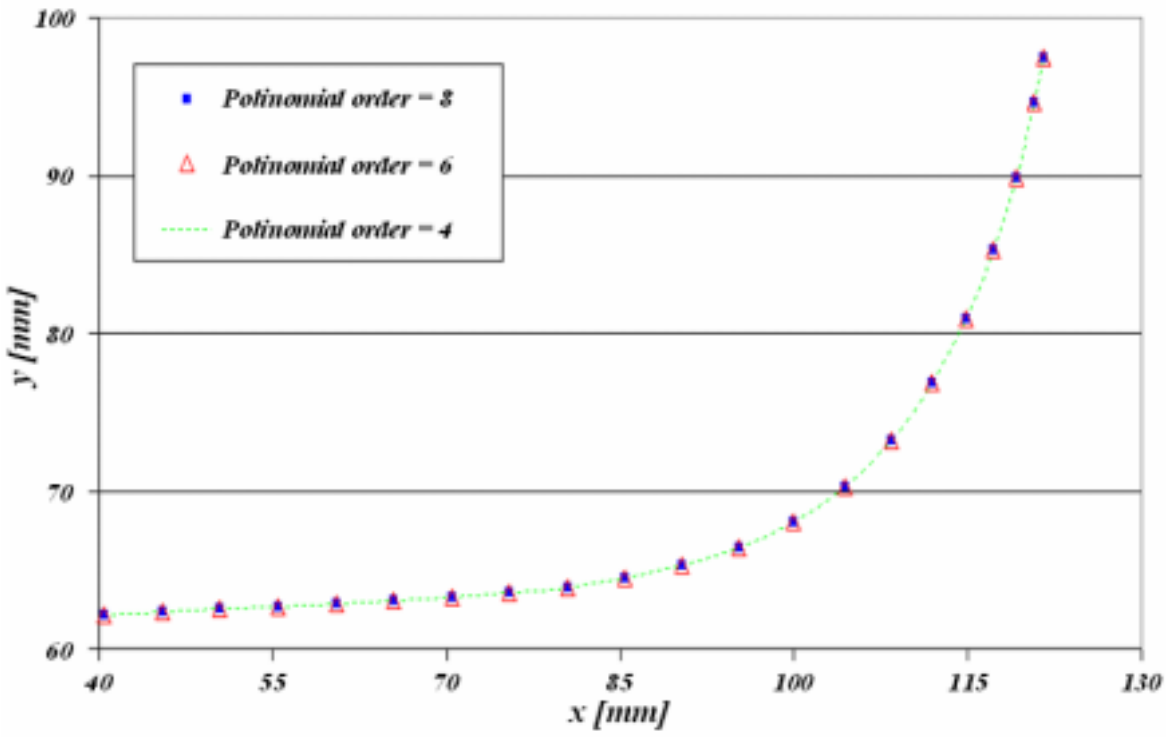

Figure 6.21. Crack path results for different polynomial order (round notch model)

Figure 6.22 plots the crack path prediction for the two notch thicknesses, $h_c = 0.03$ and 1 mm. As can be observed there is a small influence on the crack path prediction for the *DCB*. However, the existence of a gap was crucial for crack turning. It should be reminded that no gap opening generated no crack turning when using first order criteria as represented in Figure 6.7.

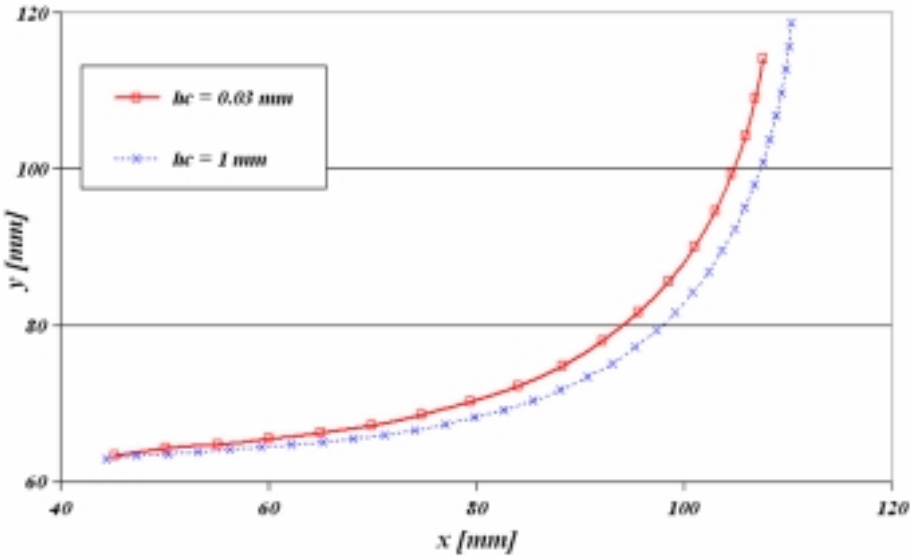

Figure 6.22. Crack path predictions on DCB for different notch thicknesses (round notch model)

The crack paths, obtained with the notches described in Figure 6.15, are depicted in Figure 6.23. A gap opening of the notch equal to *1* mm was used for the plotted simulation results.

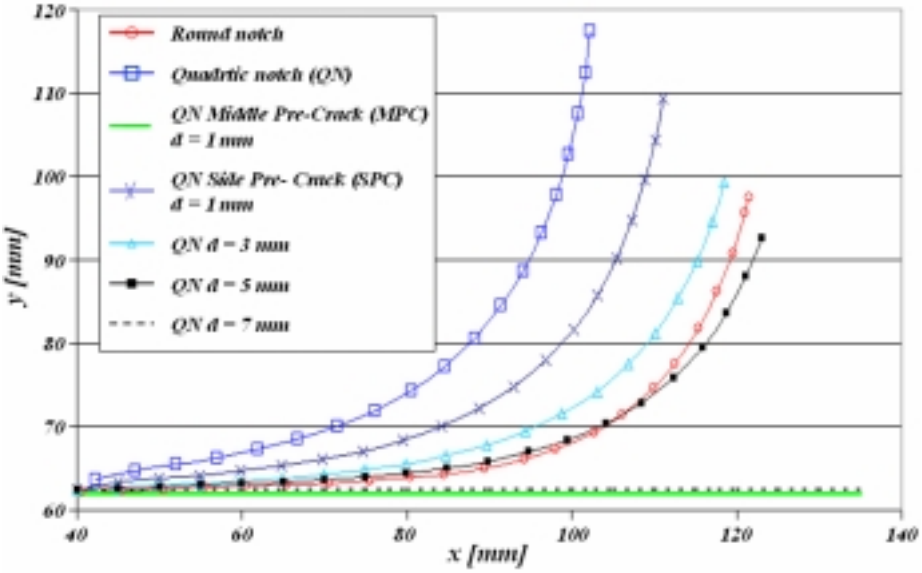

Figure 6.23. Automatic crack path prediction on DCB for different notch geometries and pre-crack lengths with $h_c = 1$ mm

For the *CFS*-models, the number of iterations was selected to be 80 and the maximal crack length was set to *400* mm.

The resulted crack paths obtained with the different *CFS*-models are illustrated in Figures 6.24 and 6.25 for a notch gap equal to *1* mm and a crack increment of *5* mm.
The crack path obtained on the experimental results of testing is also included in these figures.

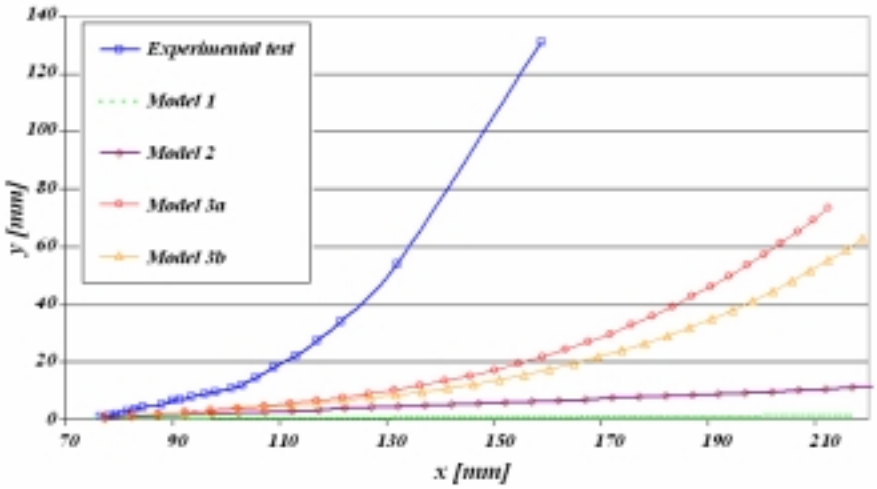

Model 1. Half without arms	***Model 2: Half with arms***
Model 3a: Complete without details	***Model 3b: Complete with filled details***

Figure 6.24. CFS-crack path predictions using model 1 until model 3b with a notch gap of 1 mm

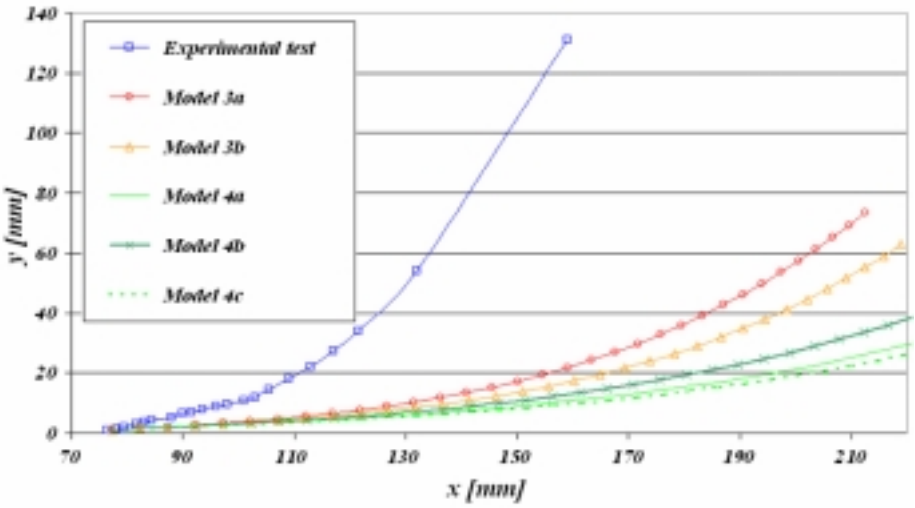

Model 3a: Complete without details	***Model 4a. Complete with simple groves***
Model 3b: Complete with filled details	***Model 4b: Complete with internal rounded groves***
	Model 4c: Complete with external rounded groves

Figure 6.25. CFS-crack path predictions using model 3a until model 4 with a notch gap of 1 mm

Finally, Figures 6.26 and 6.27 illustrate the obtained crack paths on model 2 and model 3a respectively for different notch gaps including the obtained crack path from experimental results.

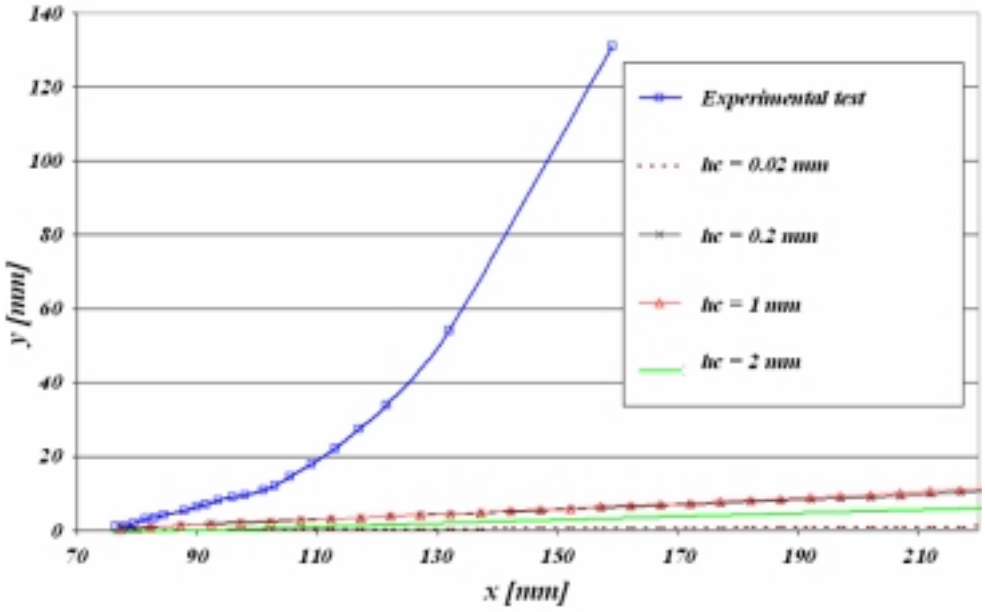

Figure 6.26. CFS-crack path predictions using model 2 and different notch gaps

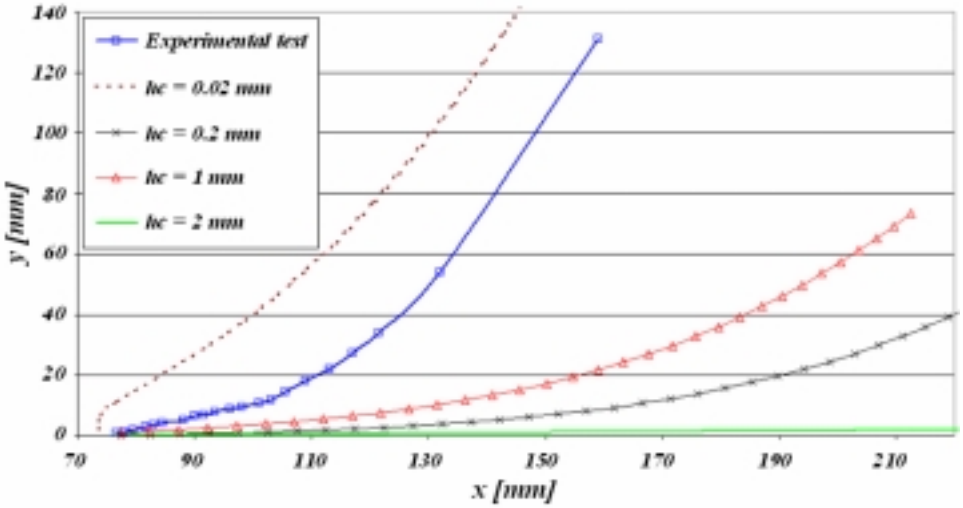

Figure 6.27. CFS-crack path predictions using model 3a and different notch gaps

The following statements can be concluded concerning the crack path prediction under pure *Mode I* loading from the above illustrated results.

a) The selected crack increment, Δa, has usually low influence on the predictions, unless the crack approaches a stress concentration item (e.g. hole, edge, change of thickness, etc.). In this case the selection of the crack increment is critical since it may determine whether the crack

is subjected to the stress concentration field of the item. Therewith, two very different crack paths and corresponding failures may result. However, as long as there is no such stress concentration item, different crack increments will tend to induce the same crack path.

b) As already mentioned, the high polynomial order used was not needed since the convergence of the solution is already reached with a polynomial of order of four. The reason for this was that the generated mesh was dense enough to delivery an accurate result.

c) As can be observed in Figures 6.24 and 6.25 the selection of the model to represent the actual specimen or component had an important effect on the crack path calculation.

d) The modelling details, as the gap opening of the notch, had a relevant importance on the prediction of the crack path. Furthermore, the effect of the gap opening was found to depend on the model, as observed in Figures 6.26 and 6.27.

In order to analyse more deeply the influence of the notch gap and the pre-crack position and length, a full *2D*-model were generated with StressCheck® and manual mesh. The boundary conditions and loads are defined in Figure 6.28. The number of elements was about 840.

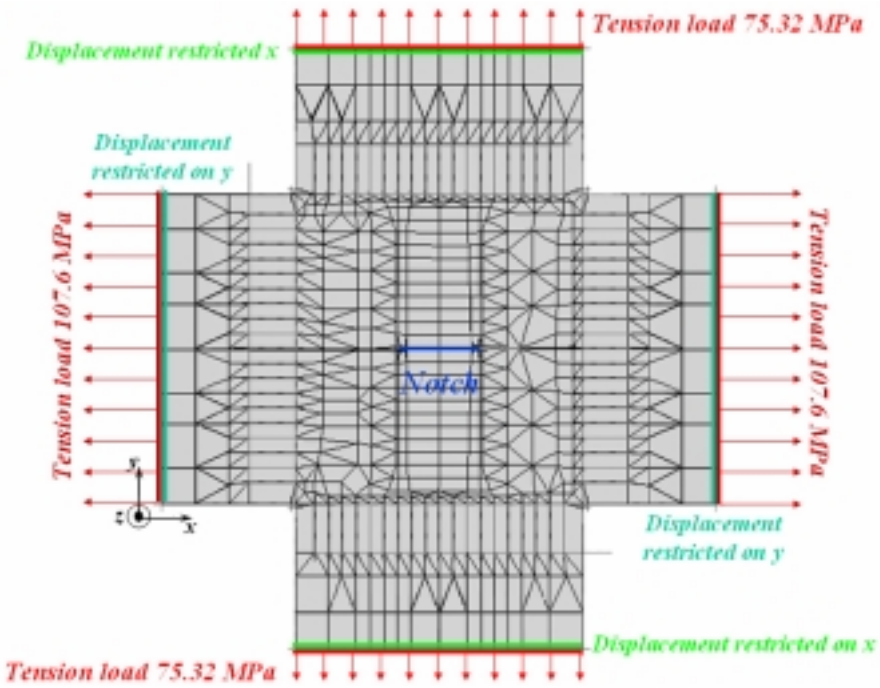

Figure 6.28. Manual mesh and boundary conditions of the CFS-model

Two different crack positions were modelled as depicted in Figure 6.29. The models were fracture-analysed extracting the *SIF* and the *T*-stress for crack lengths, *d*, between *5* and *50* mm and for five different gap openings of the notch, h_c = *0*, *0.02*, *0.2*, *1* and *2* mm.

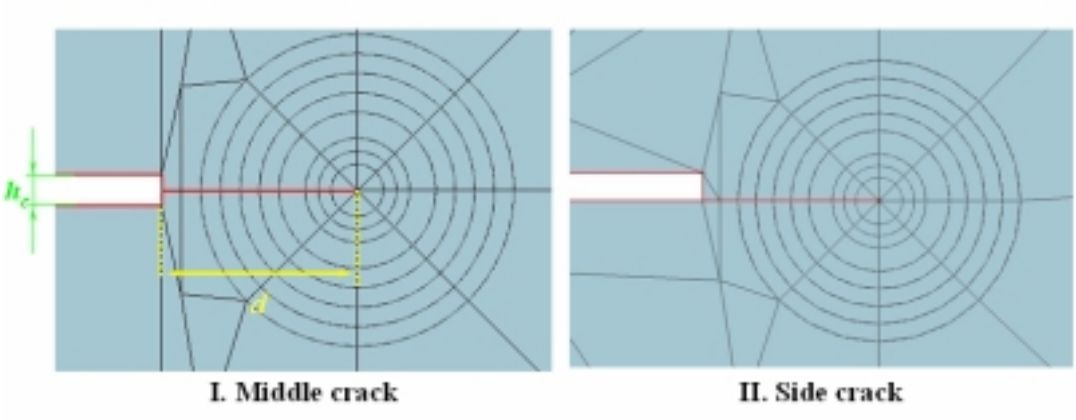

Figure 6.29. Modelled crack tip positions

The radii of the path-integral to compute the *SIF* and the *T*-stress were selected to be situated on the fourth element circle from the crack tip in order to avoid oscillations on the values of the parameters.

The results are plotted in Figures 6.30 to 6.33 for the middle crack and the side crack respectively.

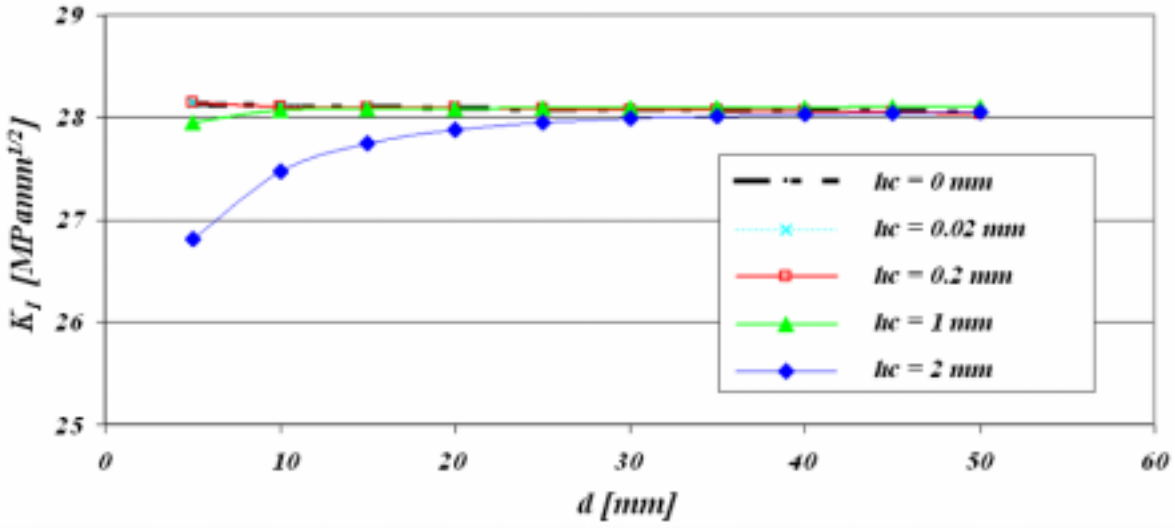

Figure 6.30. Stress intensity factor under Mode I for the crack situated on the middle of the notch (I. Middle crack)

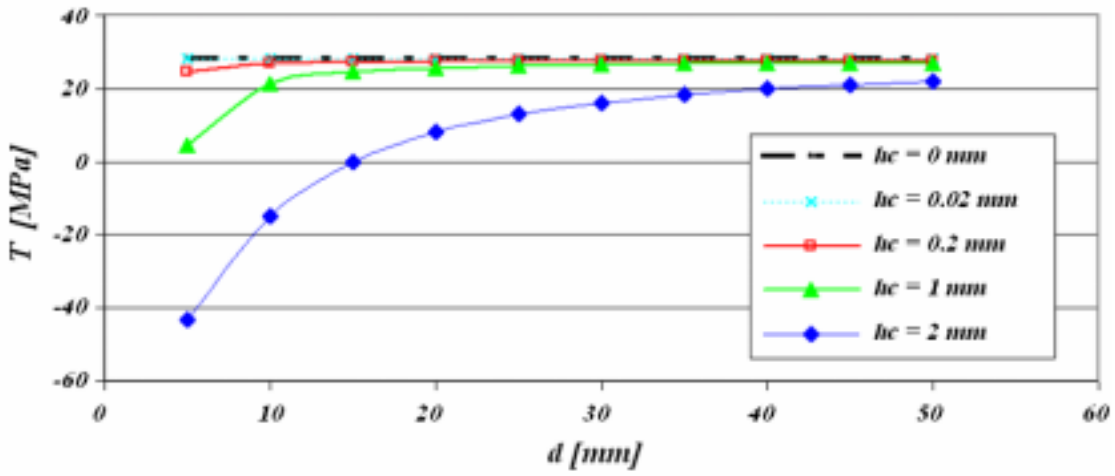

Figure 6.31. T-stress for the crack situated on the middle of the notch (I. Middle crack)

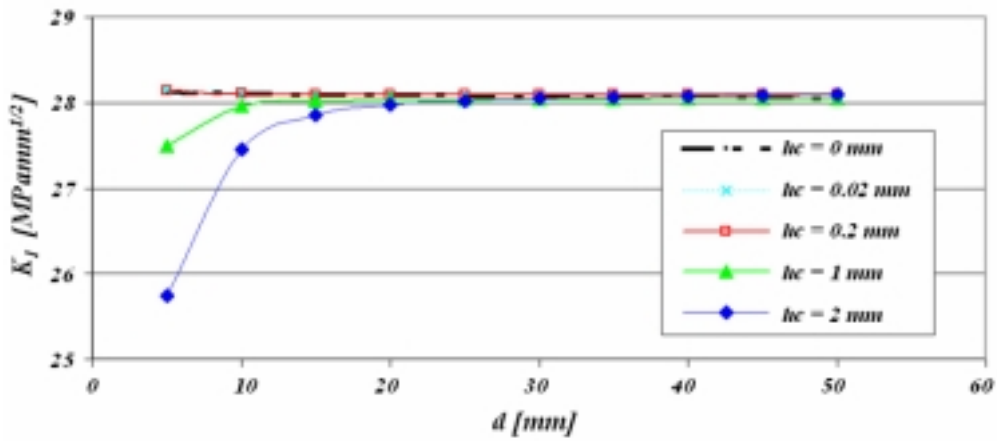

a)

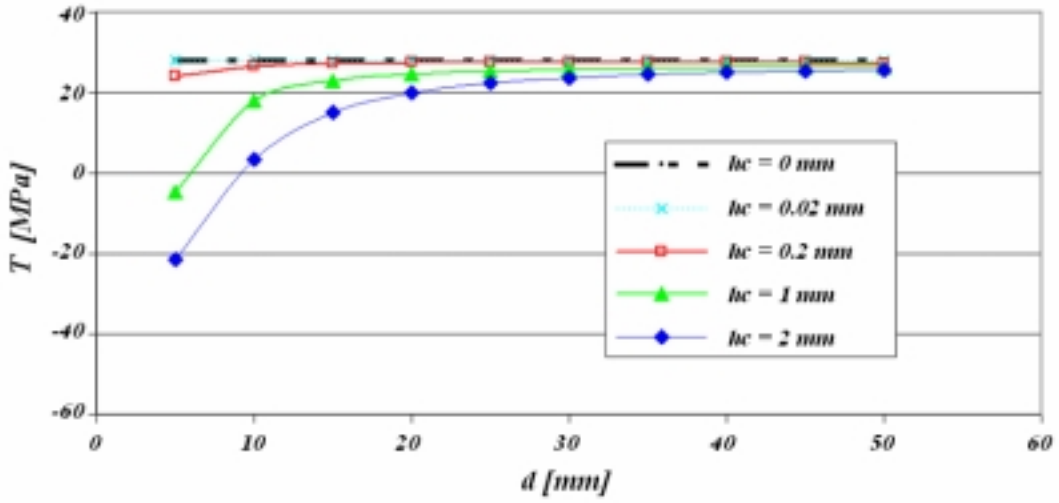

b)

Figure 6.32. a) Stress intensity factor under Mode I and b) T-stress for the crack situated on the side of the notch (II. Side crack)

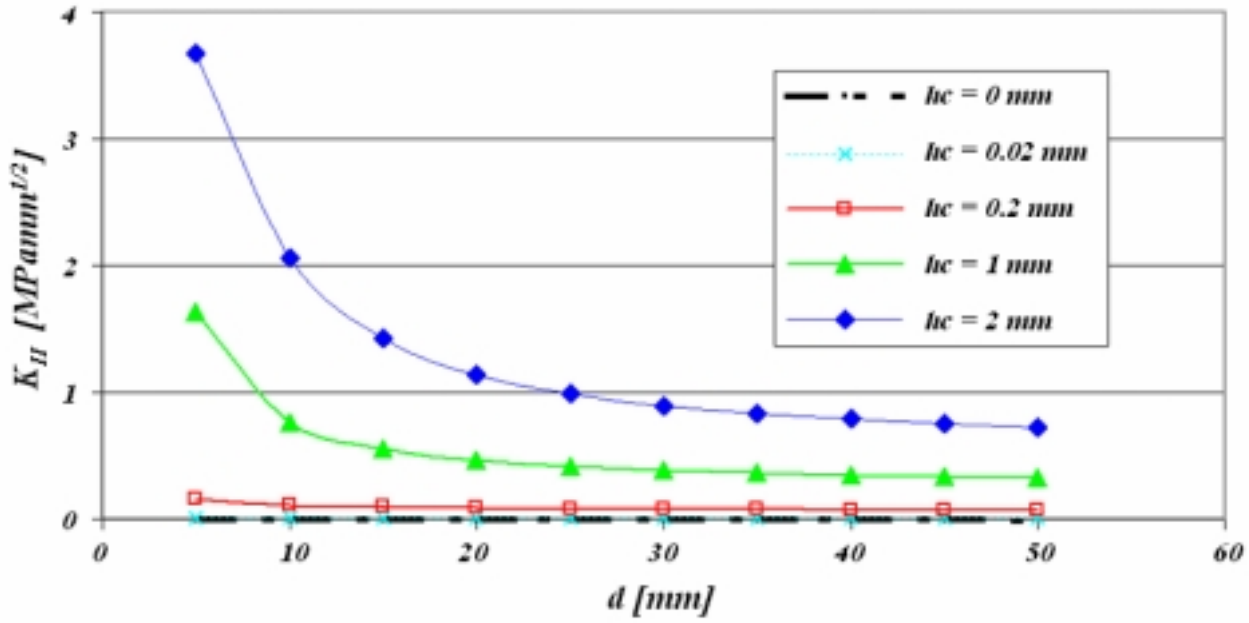

Figure 6.33. SIF under Mode II for the crack situated on the side of the notch (II. Side crack)

From the above results the following conclusions were drawn:

a) The effect of h_c on the crack tip stress field decreased as the crack length increased, i.e. as the distance to the notch increased.

b) The opening gap of the notch reduced the *SIF* under *Mode I* and the *T*-stress for both crack positions. This effect was stronger near the notch. On the other hand, the *SIF*-component for *Mode II* was increased by a higher h_c for the side modelled crack.

c) As expected, the model with the side crack generated a K_{II} component. This was produced because the structure was no longer symmetric, the crack was no more at the centre line, $y = 62$ mm, and therefore some bending was introduced.

It was observed that when varying the values of the stresses perpendicular and parallel to the crack plane, the former contributes to both K_I and T, while the later contributes only to T, as it is well known in the literature [58].

The effect of crack position and the gap of the notch have a capital importance on K_I, K_{II} and T and consequently for the crack turning predictions. It has to be recalled that K_{II} is the responsible

of crack turning for the first order criteria and the ratio K_I/T defines, on second order criteria, the moment that crack turning will take place.

6.2.3 Explanation for the observed crack propagation behaviour

Thanks to the performed simulations, some behaviour observed on the experimental results of testing reference RU04 can be now explained.

The fact that under quasi-static load the crack turned sharply with higher notch lengths and the crack turning was larger than under cyclic loading is attributed to the *T*-stress. Higher loads produce higher *T*-stress and this stress is also increased by longer crack lengths.

The existence of a saturation notch length for crack turning, that is, a crack length which is no more influenced by the anisotropy, can be explained in terms of the *T*-stress. In other words, for large notch lengths the crack paths in T-L and L-T tend to be equivalent. Defining $\sigma_T = T - \sigma^{\infty}$, where σ^{∞} is the far field stress normal to the crack, and according to literature and experimental observations which agrees that the crack usually propagates perpendicular to the maximal applied stress, when σ_T approaches the ultimate tensile strength of the material, R_m, the crack will grow unstable approximately perpendicular to σ_T if $\sigma^{\infty} << R_m$ [23].

6.3 Results from the test-set reference DE05

The experimental test results of the ref. DE05 revealed that the notch geometry had less influence on the crack turning than predicted by the simulations performed in section 6.2.2 as observed in Figure 6.34. This shows that some assumptions, taken during the modelling of the *DCB*-specimens in the last section, were not exact.

The following conclusions can be made on the basis of Figure 6.34:

a) The inclination of the crack front (angle ψ) has no effect on the crack path. This agrees with the results simulated in section 6.2.1.

b) All crack paths created under quasi-static or cyclic loading revealed the same trend (similar paths) independently of the notch length (i.e. *33*, *38* or *43* mm), notch gap and notch inclination.

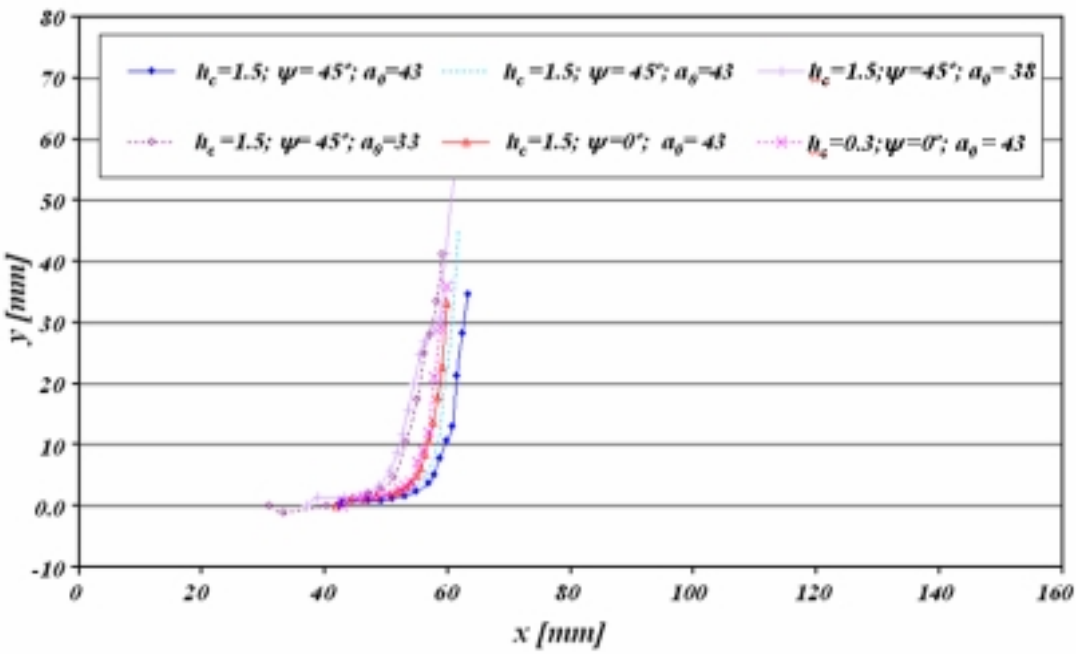

Figure 6.34. Crack paths form the experimental results of testing ref. DE05 with different notch characteristics: h_c = 1.5 or 0.3 mm, Ψ= 0º or 45º and notch lengths: a_0 = 43, 38 or 33 mm

c) Under quasi-static loading the crack turned earlier (lower *x*-coordinate) than under cyclic loading.

d) The analyses carried out by means of ARAMIS, illustrated in Figures 4.30 and 4.31 and summarised in Figure 6.35, show that a high degree of plastification takes place only at small distance from the crack tip for both quasi-static and cyclic loading. In other words, the plastic deformation was contained in a small local zone. However, only the area directly at the crack tip was analysed by ARAMIS and not the whole specimen. This means that the use of *LEFM* for crack propagation analyses is justified only regarding the crack tip plastification, which is one of the two necessary conditions to use *LEFM*. It should also be proved that the rest of the ligament remains under elastic conditions. This analysis is discussed in section 6.5.

It should be noted that the red colour behind the crack tip was not generated by higher constrains but by the opening of the crack edges.

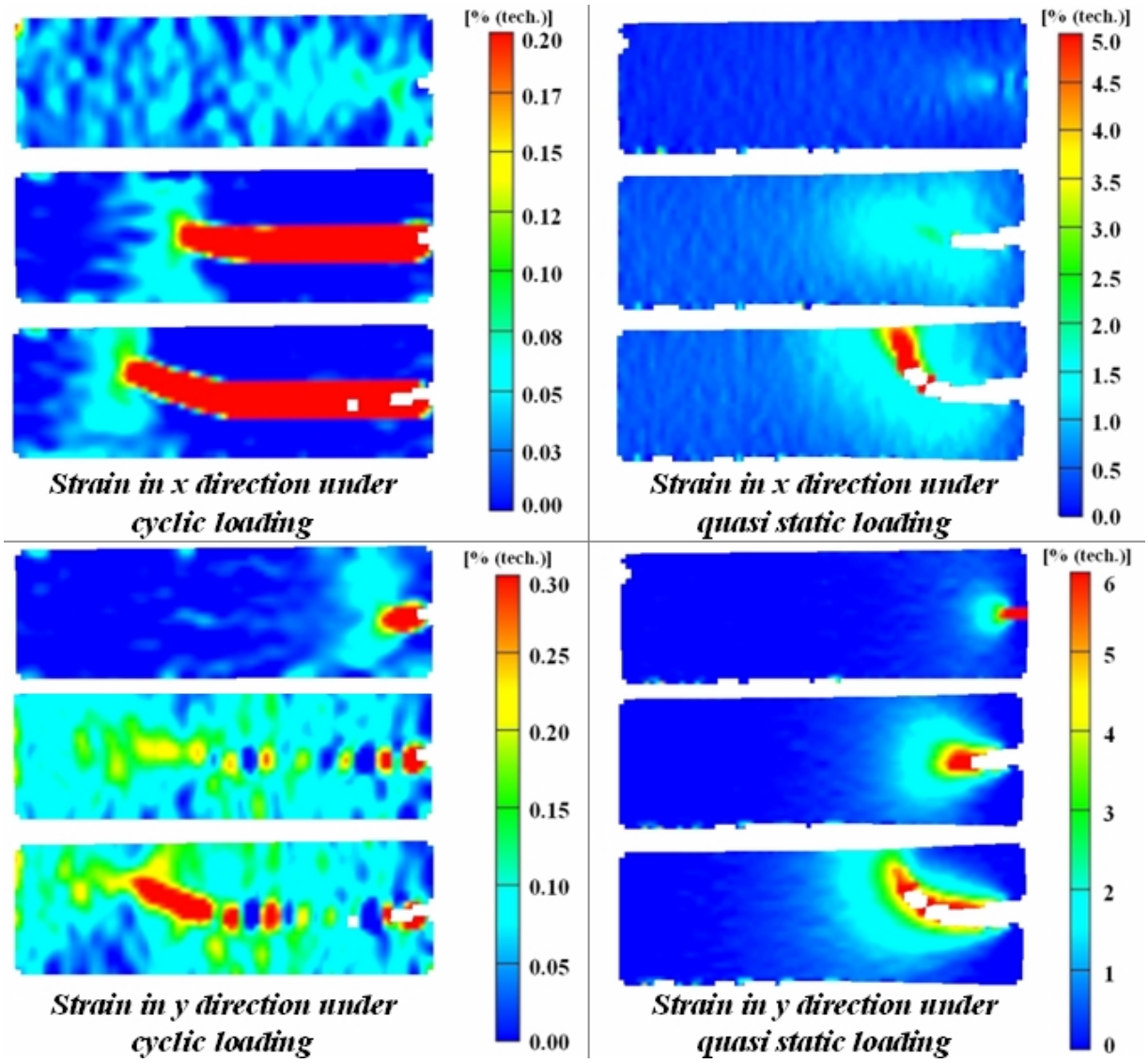

Figure 6.35. Summary of Figures 4.30 and 4.31; Strain at the crack tip analysed by means of ARAMIS

e) As observed in Figure 6.35, the plastic zone under quasi-static loading was about twenty times larger than under cyclic loading. Therefore, it is also expected that the rest of the specimen will earlier show plastification for a specimen charged under quasi-static than under cyclic loading.

6.3.1 Direction of extrusion

An analysis of the microstructure was carried out with a Leica Polyvar SC optical microscope on the *DCB*-specimen to identify the extrusion direction, L. The clad coating was removed with a caustic solution described in [S9]. The structure was analysed on different directions and the observations were assembled on a cube representation as shown in Figure 6.36.

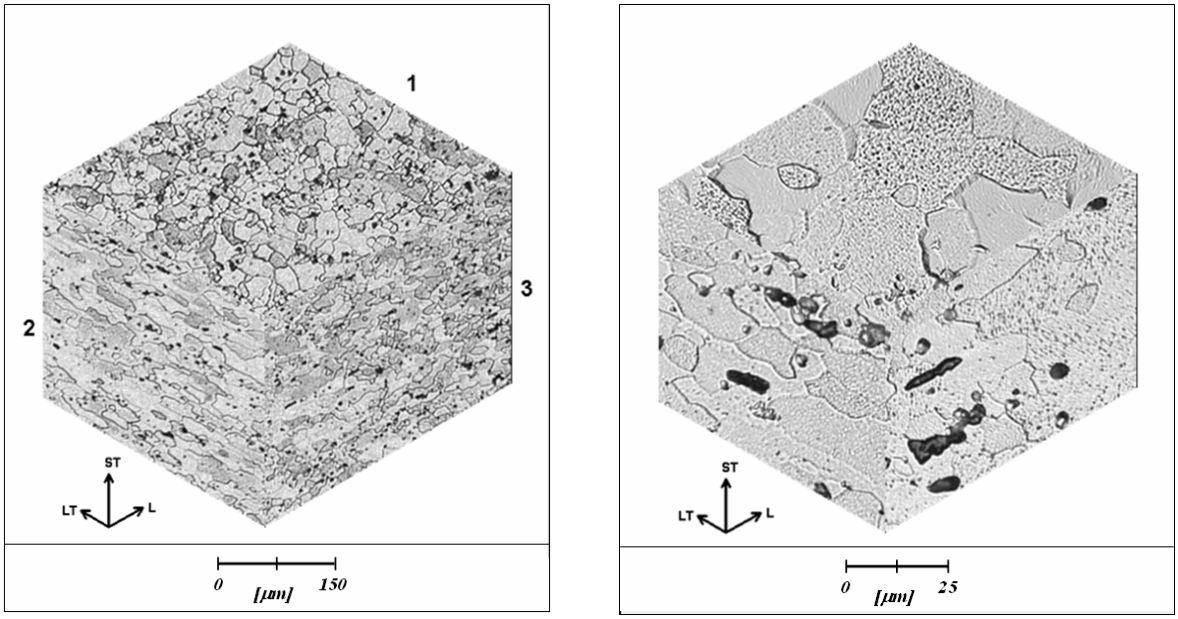

Figure 6.36. Cube representation of the delivered sheet 2024-T3 analysed by means of an optical microscope

Side 1 corresponds to the plate surface, side 2 is parallel to the extrusion direction and side 3 is perpendicular to the extrusion direction.

According to this analysis, the length and the cut of the notch on the *DCB*-specimen correspond to the direction of extrusion, i.e. the fracture mechanics orientation is the L-T.

6.3.2 COD-F-Crack length

In this section the simulation process performed in section 6.1.1 is evaluated by means of the results of the test ref. DE05. To carry out the evaluation, the applied force and the crack opening displacement were recorded automatically during the crack propagation under quasi-static loading and represented graphically, as the chart in Figure 6.37.

The relation between applied force and crack tip position was monitored by means of a travelling microscope with a magnification of 50x. Approximately thirty values of force vs. crack position per tested specimen were recorded. The plastification of the crack tip for four of the tested specimens was analysed using the ARAMIS cameras. To measure the plastification, the test was held on for few seconds maintaining the applied force. During this time a picture of the selected area of the specimen was taken with both ARAMIS cameras.

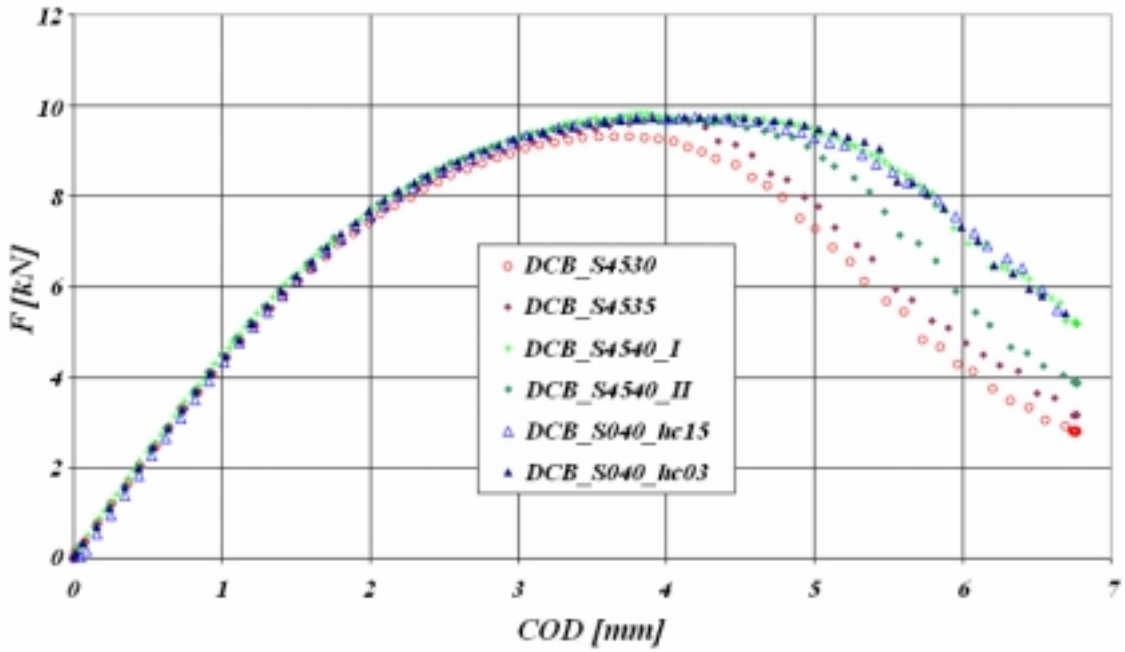

Figure 6.37. Force vs. COD records for the DCB-specimens tested under quasi-static loading

Examples of the treated images captured with ARAMIS can be seen in Figure 6.35. Table 6.5 shows an example of the recorded data for the DCB_S4540_II specimen (notch length = *43* mm, $\psi = 45^{o}$ and $h_c = 1.5$ mm). The data of all specimens tested under quasi-static loading are plotted in Figure 6.38. Δx defines the relative crack extension on the *x*-axis.

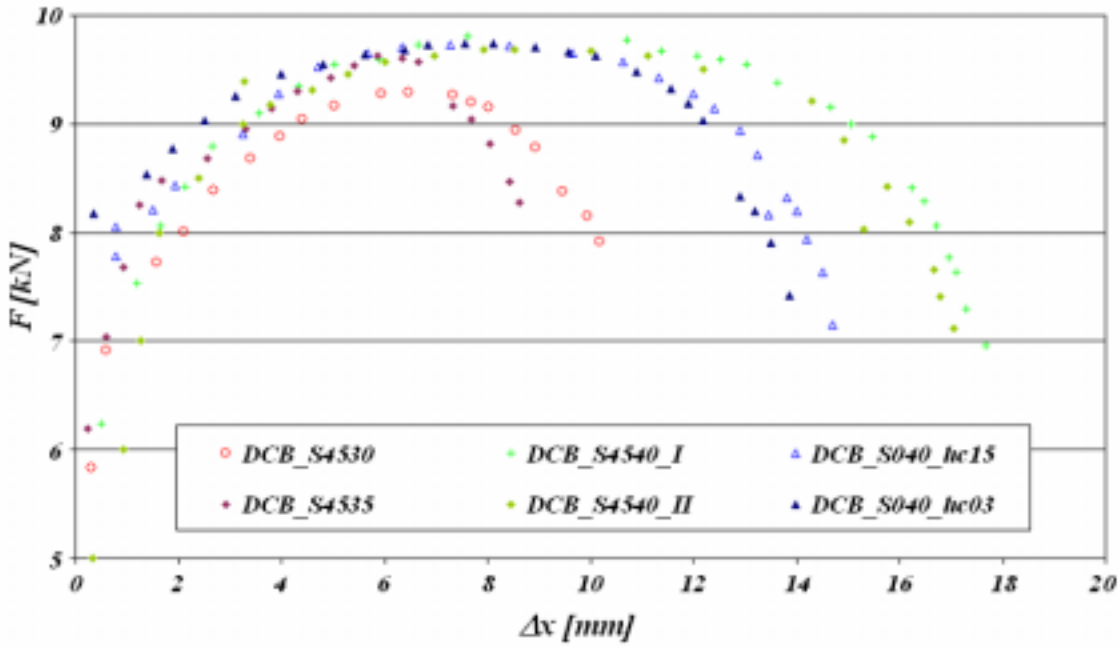

Figure 6.38. Force vs. crack propagation for the specimens tested under quasi-static loading (test ref. DE05)

Combining the curves depicted in Figure 6.38 a master curve was created. This was used to calculate the applied force on the *40* mm notched *DCB*-model at each crack tip position.

Table 6.5. Example of the notes recorded from specimen DCB_S4540_II

Force [N]	*Crack position x-coordinate [mm]*	*Crack position y-coordinate [mm]*	*ARAMIS pictures*
2500	*0.00*	*0.00*	*1st Shoot*
4000	*0.15*	*0.34*	*2nd Shoot*
5000	*0.33*	*0.53*	*3rd Shoot*
6000	*0.93*	*0.60*	*4th Shoot*
7000	*1.27*	*0.70*	*5th Shoot*
8000	*1.64*	*0.83*	*6th Shoot*
8500	*2.39*	*1.12*	
9000	*3.26*	*1.34*	*7th Shoot*
9180	*3.78*	*1.39*	
9315	*4.61*	*1.49*	
9465	*5.30*	*1.68*	
9567	*6.01*	*1.85*	*8th Shoot*
9634	*6.96*	*2.05*	
9683	*7.94*	*2.30*	
9680	*8.53*	*2.62*	*9th Shoot*
9675	*10.02*	*2.97*	
9626	*11.12*	*3.35*	
9505	*12.19*	*3.88*	*10th Shoot*
9395	*13.27*	*4.42*	
9214	*14.29*	*5.52*	
8850	*14.92*	*6.76*	*11th Shoot*
8030	*15.31*	*7.73*	
8419	*15.75*	*8.66*	*12th Shoot*
8100	*16.20*	*10.17*	
7655	*16.68*	*11.80*	*13th Shoot*
7410	*16.79*	*13.04*	*14th Shoot*
7120	*17.05*	*14.26*	
3870	-	-	-

Additionally, the crack paths measured during the experimental test for the *40* mm notched specimens were averaged.

A *DCB*-specimen with a *40* mm notch was modelled with the averaged crack path. The simulations were carried out as described in section 6.1.1. Seven different crack tip positions were analysed. It should be taken into account that for each crack tip position a geometric non linear-elastic analysis was performed with force magnitudes between *0.5* and *11* kN and the values of the *COD* at the mouth of the notch were computed and plotted for each force and crack length. In this plotting it was also included the recorded experimental values of testing (ref. DE05) force vs. *COD*. The intersections between the simulated and the experimental test curves

determined the applied force at each crack tip. Herewith the connection between force-crack length and *COD* was determined.

The master curve defined above was used to extract the recorded connections (during experimental tests) at the seven simulated crack tips. These sets of values (simulation and experimental results of testing) were compared, and with it, the simulation process was evaluated. Table 6.6 summarises this comparison.

Table 6.6. Comparison of forces determined by experimental testing (ref. DE05) and simulation for different crack lengths

	Crack tip coordinate		***F [N]***	
	x [mm]	***y [mm]***	***Experimental test***	***After simulation***
a0	68.5	62.0	-	9350
a3	75.2	61.2	9732	9732
a5	79.0	60.4	9780	9810
a7	82.9	58.3	9380	9718
a9	84.8	54.2	8883	9300
a11	86.7	48.9	7297	8062

The comparison showed very similar results between simulated and recorded forces. Larger deviations were observed for longer cracks. The reason lied in the increase of global plastification: *DCB*-specimens with longer cracks generate higher moments and higher displacements. These displacements produce small plastic deformation at the edges that influence the crack path.

Herewith the simulation process to evaluate the connection between *COD*, force and crack tip positions was corroborated. This validates the results obtained in section 6.1.1.

6.4 Boundary conditions study

As already remarked, all crack paths on the test referenced DE05 charged under cyclic or quasi-static loading were independent on the notch lengths, opening gaps of the notches and inclinations of the notches. This information leads to the conclusion that the predictions of crack paths performed until now failed due to disagreement with the applied boundary conditions during testing. In order to better reproduce the testing situation, the experimental test was meticulously analysed.

From this analysis, different possible boundary conditions were conceived always respecting the minimal conditions needed to perform a correct simulation.

The principal characteristics of the boundary conditions for the *DCB*-specimen in agreement with the test (reference DE05) are listed below.

a) The end of the specimen was never constrained, as opposed to the configuration simulated until now.

b) The pin at the upper hole was fixed, while the pin at the lower hole was pulled.

c) The restriction of the movement taking place between the upper pin and the upper hole of the specimen was produced with a part of the upper and left side of the hole.

d) There was a movement restriction on the lower hole of the specimen due to the lower pin. The contact zone between the pin and the specimen was situated at the left side of the specimen hole.

The same *FE*-model as in Figure 5.15, but constrained with different boundary conditions representing the above observed movement restrictions was analysed. The restrictions were applied locally on nodes, or more extended on edges and they were completely fixed, i.e. no movement allowed, or partially fixed. The partial fixation took place by means of distributed springs. The value of the spring coefficient was calculated by the ratio between the modulus of elasticity and the thickness of the specimen.
The spring constraint fixes the object on the selected zones until a determined force is reached. Displacements are allowed for positive increments (applied force minus limit force of the spring).

These studies were performed on the specimens with *40, 90* and *140* mm notch lengths. The models were generated with StressCheck® in *2D*. The number of elements was between 120 and 150.

The different modes used to constrain the specimen are represented in Figures 6.39 and 6.40.

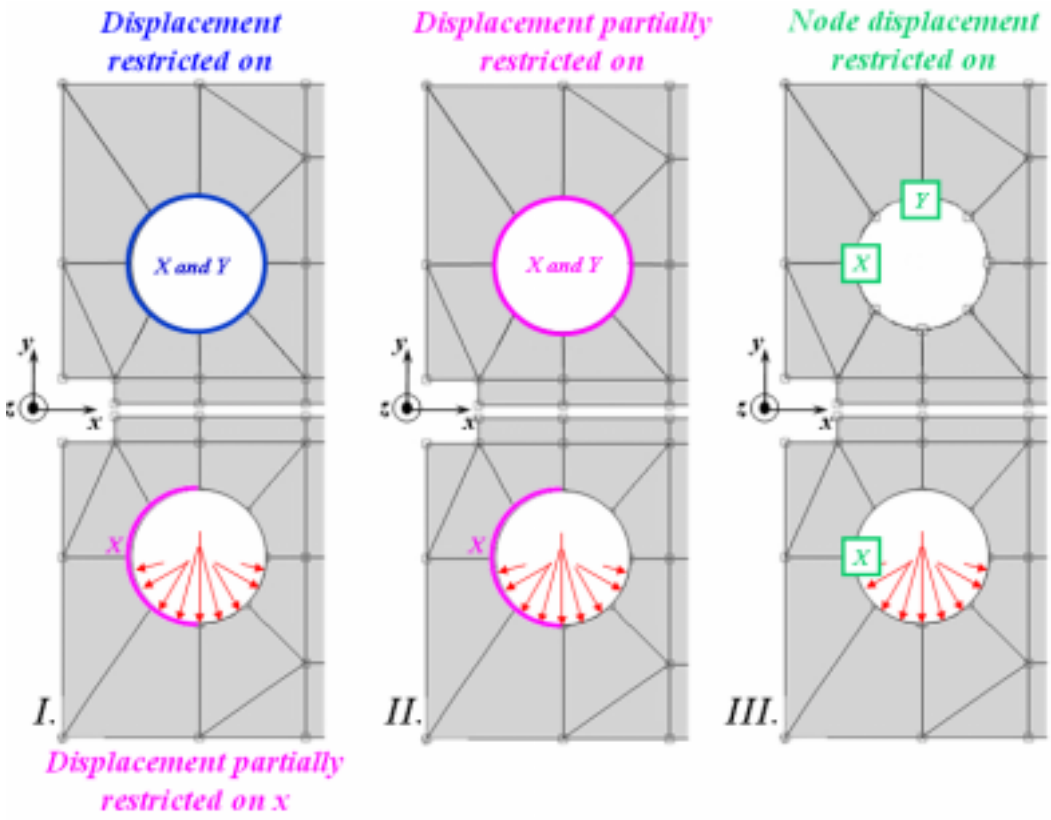

Figure 6.39. Displacement restrictions applied on nodes or edges with partial and total fixation

Linear elastic and non-linear geometric elastic computations were performed by means of two bearing loads of *2* and *10* kN. The fracture parameters K_I, K_{II} and *T*-stress were computed at the crack tip and by means of these values the plastic length at the crack tip, r_p, the beta factor, that is, the ratio between the *T*-stress and the applied stress and the biaxial parameter, *B*, were calculated. The biaxial parameter was introduced by Leevers & Radon [55] to normalise the *T*-stress.

This is calculated by means of the crack length, the *SIF* and, of course, the *T*-stress, as shown in equation 6.4.1.

$$B = \frac{T\sqrt{\pi a}}{K_I} \quad (6.4.1)$$

Furthermore, the generated deformation of the specimen was also taken into account for the evaluation of the boundary conditions. The results corresponding to five of the boundary conditions represented in Figures 6.39 and 6.40 are given in Table 6.7, together with the results obtained from the boundary conditions used in last sections for a crack length of *140* mm.

Table 6.7. Fracture mechanics results for the boundary analysis on the DCB-specimen with a notch length of 140 mm

Boundary conditions	***F [kN]***		***K_I [MPa*m$^{1/2}$]***	***K_{II} [MPa*m$^{1/2}$]***	***T [MPa]***	***r_p [mm]***	***$K_I/\sigma(\pi a)^{1/2}$***	***T/σ***	***$B = T(\pi a)^{1/2}/K_I$***
Nodes fixation at specimen end (Fig 5.15)	***2***	***NLA***	45	0	187	0.56	3.924	11.413	2.909
		LA	44	0	190	0.56	3.921	11.578	2.953
	10	***NLA***	223	0	883	13.98	3.933	10.770	2.738
		LA	222	0	949	13.90	3.921	11.579	2.953
Upper edge fix (Fig 6.39 I)	***2***	***NLA***	34	8	127	0.33	3.004	7.753	2.581
		LA	34	8	130	0.33	3.027	7.948	2.626
	10	***NLA***	166	37	582	7.76	2.930	7.098	2.422
		LA	172	39	651	8.28	3.027	7.946	2.625
All spring conditions (Fig 6.39 II)	***2***	***NLA***	44	0	187	0.56	3.921	11.419	2.912
		LA	44	0	190	0.56	3.921	11.572	2.951
	10	***NLA***	221	-3	881	13.69	3.892	10.753	2.763
		LA	222	0	949	13.89	3.920	11.574	2.953
Fix nodes (Fig 6.39 III)	***2***	***NLA***	45	0	187	0.56	3.924	11.425	2.912
		LA	44	0	190	0.56	3.921	11.578	2.953
	10	***NLA***	222	0	884	13.87	3.917	10.779	2.752
		LA	222	0	949	13.90	3.921	11.579	2.953
Spring + 1 node (Fig 6.40 V)	***2***	***NLA***	44	0	187	0.56	3.921	11.419	2.912
		LA	44	0	190	0.56	3.921	11.572	2.951
	10	***NLA***	222	0	883	13.86	3.916	10.775	2.752
		LA	222	0	949	13.89	3.920	11.574	2.953
Edge X-Y fixed (Fig 6.40 VII)	***2***	***NLA***	35	3	130	0.33	3.040	7.912	2.602
		LA	35	3	131	0.33	3.040	7.997	2.630
	10	***NLA***	172	12	619	8.33	3.036	7.549	2.487
		LA	173	13	656	8.36	3.040	8.000	2.631

These results highlight the importance of the boundary conditions and of the variations on K_I, K_{II} and *T*-stress by non-linear geometric analyses, as observed in section 5.5.2, compared with linear analyses. The generation of *Mode II* can be related to the selected boundary conditions. Furthermore, they have an important effect on K_I and *T*-stress values.

The selection of the boundary conditions reflecting the conditions on the experimental test was done evaluating the displacements and the deformations of the specimen produced with the conditions described above. These were then compared with the deformations observed during the experimental test ref. DE05.

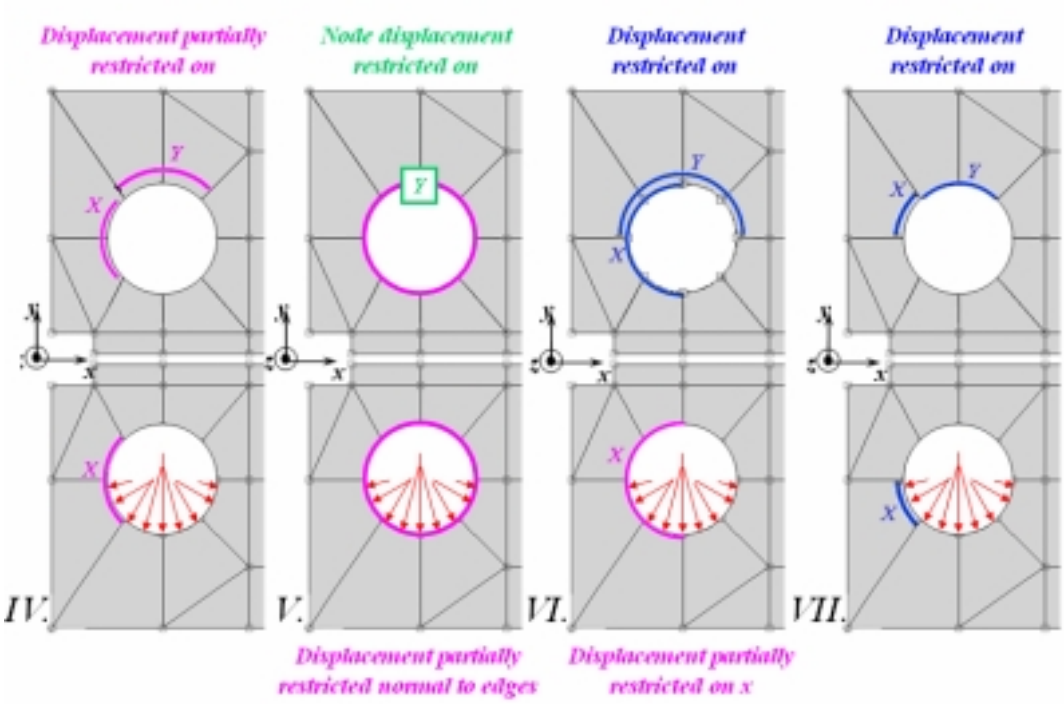

Figure 6.40. Displacement restrictions applied on nodes or edges with partial and total fixation (continuation)

Figure 6.41 illustrates the mesh and the boundary conditions which represent more precisely the displacement of the specimen obtained during experimental testing.

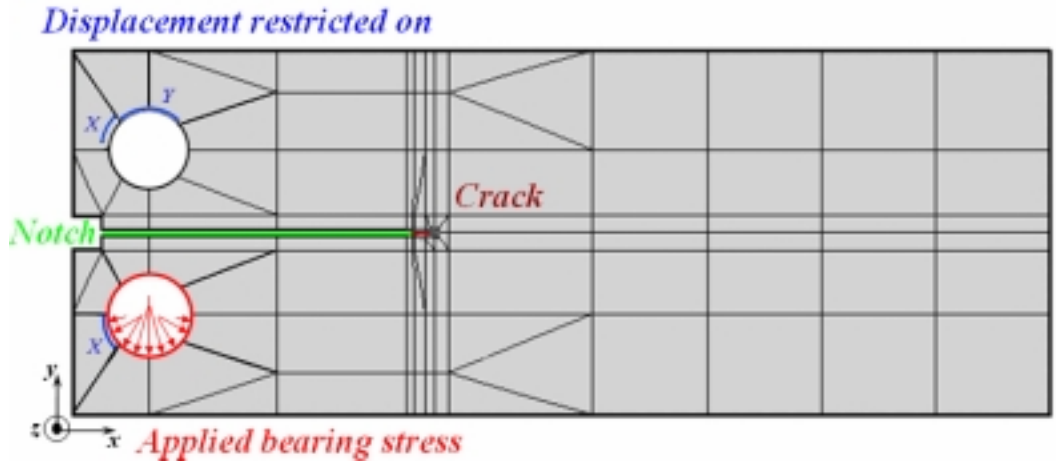

Figure 6.41. Boundary conditions in agreement with the deformations obtained on experimental tests ref. DE05

Figure 6.42 depicts the deformation of the simulated specimen with an amplification factor of 100 and the correspondent stress distribution for a crack length of *90* mm. The comparison of the deformation produced by a turned crack during experimental test with the predicted one is presented in Figure 6.43.

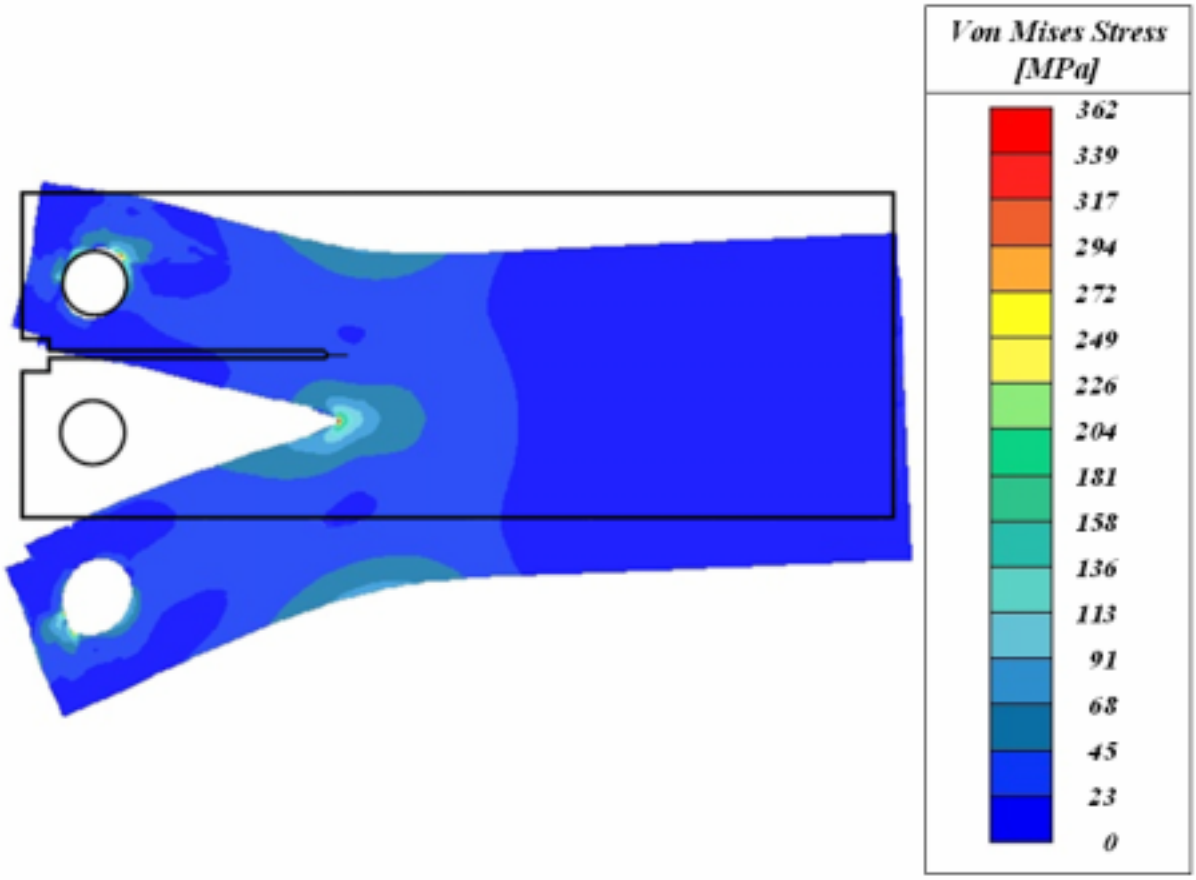

Figure 6.42. 100x amplified deformation and stress distribution for the model on Figure 6.41

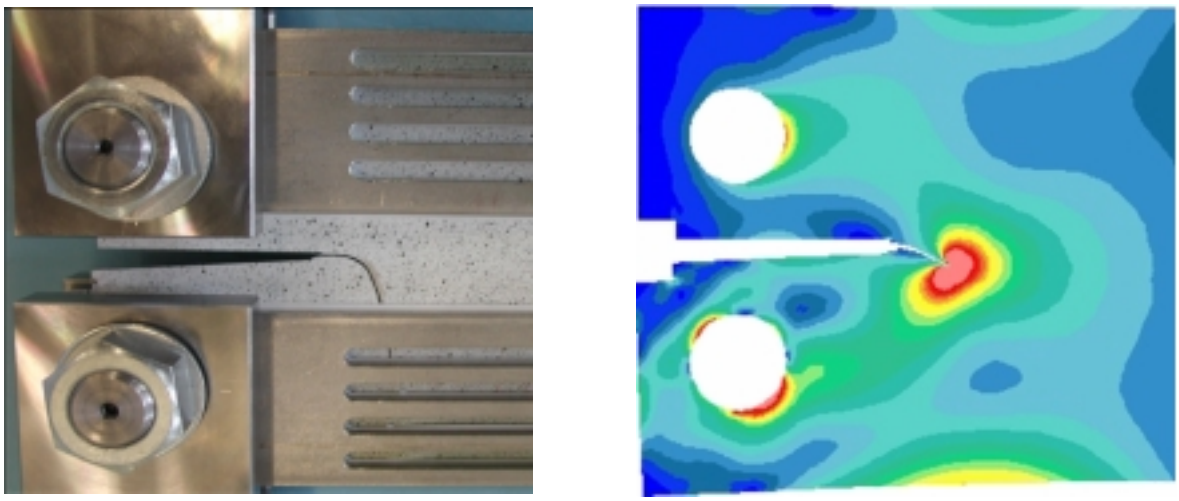

a) *b)*

Figure 6.43. DCB-specimen deformation for a turned crack path during a) experimental test ref. DE05 and b) from the simulation results

The influence that the edge at the end of the specimen has on the fracture parameters was studied for three crack lengths (*40*, *90* and *140* mm) with different specimen widths on the basis of the

boundary conditions defined in Figure 6.41. The calculated biaxial parameter versus the ratio between the ligament and the crack length are plotted in Figure 6.44.

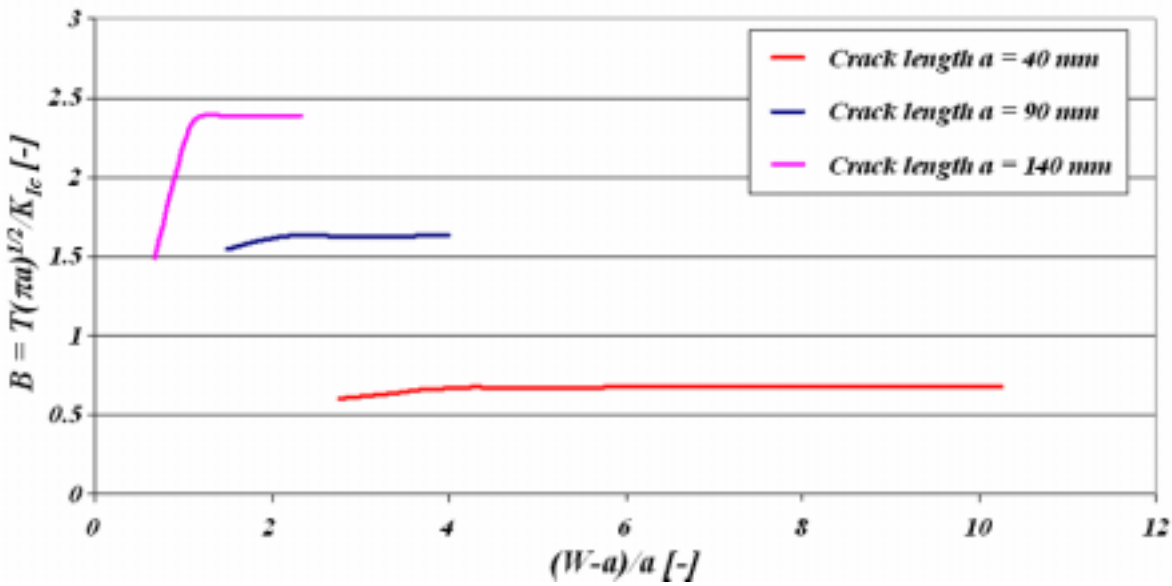

Figure 6.44. Stability of the solution varying either the crack length or the specimen width

Figure 6.44 shows that the gap of the notch influences the fracture parameters during the first millimetres of crack growth, having a major influence for small ratios between the ligament and the crack length, i.e. for crack lengths near the end edge of the specimen. This is a further proof that reflects again the importance of modelling the gap of the notch as well as the influence of the edge on the crack behaviour.

All further *DCB*-simulations were performed with the boundary conditions defined in Figure 6.41.

6.5 Global specimen plastification

Potential parameters influencing the prediction of the crack path have been analysed and determined in sections 6.2 and 6.4. Nevertheless, as discussed at the beginning of section 6.3, the plastification of the whole specimen must also be analysed.

LEFM applies when the non-linear deformation of the material is confined to a small region near the crack tip. This has already been proved by evaluating the results obtained by means of

ARAMIS, section 6.3. However, the crack tip fields could be affected by an increase in the global plastification of the specimen with the consequence that *LEFM* is no longer applicable.

To this aim different parameters found in the literature and describing the applicability limits of *LEFM* were treated for several crack lengths.

One of the evaluated parameters was the stress σ_T defined as $\sigma_T = T\text{-}\sigma^{\infty}$, were σ^{∞} describes the far field stress normal to the crack. The crack is assumed to propagate under elastic plastic conditions when this stress approaches the ultimate tensile strength of the material, R_m.

During cyclic loading, unstable fracture under *MM* near *Mode I*, i.e. $K_I >> K_{II}$, occurs when the fracture toughness, K_c, is reached [16]. By means of the equivalent stress intensity factor defined by Richard [14] in equation 2.4.15, the unstable fracture was defined when K_v reaches the fracture toughness of the material.

$$K_v = \frac{K_I + \sqrt{K_I^2 + 4\left(1.155K_{II}\right)^2}}{2}$$

To evaluate the degree of plastification in front of the crack tip and in the ligament, two parameters were used. Thus, L_{rp}, defined as the ratio between the equivalent stress and the elastic limit in front of the crack, was used:

$$L_{rp} = \frac{\sigma_e}{R_{p0.2}} \quad (6.5.1)$$

The other parameter was L_{rv}, which is defined as the ratio between the equivalent stress and the ultimate tensile strength at the ligament of the specimen, that is,

$$L_{rv} = \frac{\sigma_e}{R_m} \quad (6.5.2)$$

This parameter was used to control static fracture produced when the ultimate tensile strength is exceeded.

The parameters, σ_T and K_v, were evaluated at the crack tip, whereas the last two, i.e. L_{rv} and L_{rp}, were evaluated at the crack tip and on seven further positions situated on the path to be followed by the crack.

The applicability limit of *LEFM* was defined when $L_{rv} \geq 1.0$ at any point along the ligament. Furthermore, Plastic Collapse (*PC*) was defined as the stress at which irrecoverable plastic deformation starts. This was assumed when $\sigma_T \geq R_m$, $K_v \geq K_{Ic}$ or the whole ligament presented $L_{rp} \geq 1.0$. From this point on, the failure of the specimen is characterised by unstable fracture, and complete failure of the specimen takes place.

These studies were performed on the specimens with *40*, *90* and *140* mm notch lengths. The models were generated with StressCheck® in *3D*. The simulations were performed for both quasi-static and cyclic loading. For quasi-static loading, the force was adapted for every crack length according to sections 6.1.1 and 6.3.2.

A representation of the obtained results is summarised in Figure 6.45, which illustrates the plastic degree of the ligament, and Tables 6.8 to 6.10 which show the values of the different parameters described above along the crack path.

The material parameters for the *AA* 2024-T3 were *435* MPa for R_m, *110* MPa*m$^{1/2}$ for K_c and *305* MPa for $R_{p0.2}$ according to [S8].

Table 6.8. σ_T and K_v calculations for different points at the crack path for the specimen DCB_S4540 loaded under quasi-static loading

	a_3	a_5	a_7	a_9	a_{11}	a_{13}
K_I [MPa*m$^{1/2}$]	85	92	95	85	78	151
K_{II} [MPa*m$^{1/2}$]	1	2	10	21	17	35
T [MPa]	443	444	421	396	356	796
K_v [MPa*m$^{1/2}$]	85	92	96	91	83	161
σ^{∞}	78.5	78.9	75.6	71.6	58.8	40.3
$\sigma_T = T - \sigma^{\infty}$	364.2	364.8	345.2	324.8	297.4	755.9
$K_v < K_c$	True	True	True	True	True	False
$\sigma_T < R_m$	True	True	True	True	True	False

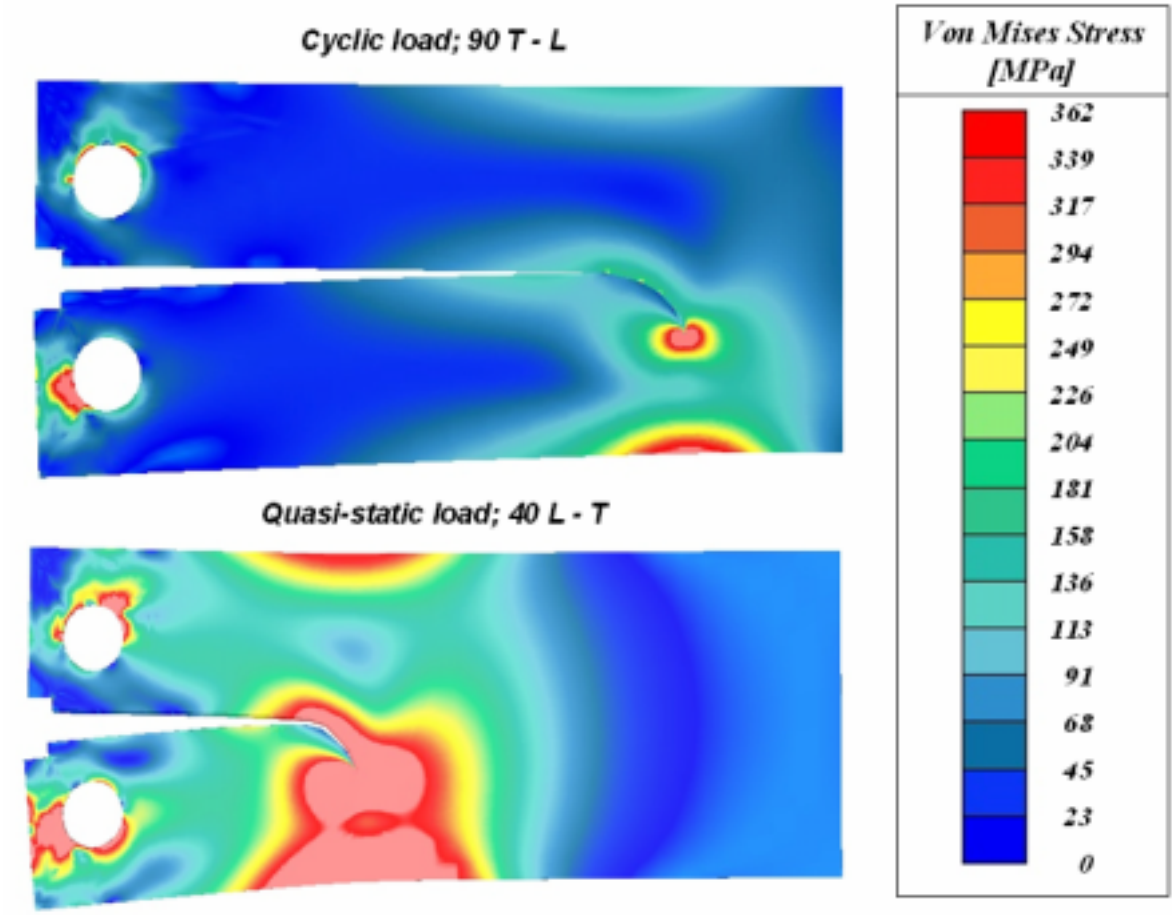

Figure 6.45. Visual degree of plasticity for two representative DCB-specimens. The illustration below (Static 40 L-T) corresponds to an applied force of 10 kN to illustrate the meaning of plastic collapse

Table 6.9. L_{rp} calculations for the DCB_S4540 specimen

	$L_{rp}=\sigma_e/R_{p0.2}$							
Crack tip at	a_3	a_5	a_7	a_9	a_{11}	a_{13}	a_{14}	***Edge***
a_3 Font	73.04	1.93	3.29	0.99	0.74	0.38	0.36	1.09
a_3 Back	87.50	1.98	6.54	1.01	0.74	0.38	0.36	1.10
a_5 Front	-	68.51	4.92	1.28	0.88	0.42	0.39	1.22
a_5 Back	-	90.38	12.73	1.31	0.89	0.43	0.39	1.23
a_7 Front	-	-	67.35	1.89	1.11	0.48	0.43	1.33
a_7 Back	-	-	94.33	1.96	1.14	0.49	0.43	1.34
a_9 Front	-	-	-	72.49	1.60	0.57	0.48	1.47
a_9 Back	-	-	-	90.96	1.67	0.60	0.49	1.47
a_{11} Front	-	-	-	-	67.22	0.68	0.50	1.48
a_{11} Back	-	-	-	-	89.16	0.71	0.53	1.47
a_{13} Front	-	-	-	-	-	99.91	2.21	3.91
a_{13} Back	-	-	-	-	-	118.69	2.48	3.88

Table 6.10. L_{rv} calculations for the DCB_S4540 specimen

	$L_{rv}=\sigma_e/R_m$							
Crack tip at	a_3	a_5	a_7	a_9	a_{11}	a_{13}	a_{14}	***Edge***
a_3 Font	51.21	1.36	2.31	0.70	0.52	0.27	0.26	0.77
a_3 Back	61.35	1.39	4.58	0.71	0.52	0.27	0.25	0.77
a_5 Front	-	48.04	3.45	0.90	0.62	0.29	0.28	0.86
a_5 Back	-	63.37	8.92	0.92	0.62	0.30	0.28	0.86
a_7 Front	-	-	47.23	1.33	0.78	0.34	0.30	0.94
a_7 Back	-	-	66.14	1.37	0.80	0.35	0.30	0.94
a_9 Front	-	-	-	50.82	1.12	0.40	0.33	1.03
a_9 Back	-	-	-	63.78	1.17	0.42	0.34	1.03
a_{11} Front	-	-	-	-	47.13	0.47	0.35	1.04
a_{11} Back	-	-	-	-	62.51	0.50	0.37	1.03
a_{13} Front	-	-	-	-	-	70.05	1.55	2.74
a_{13} Back	-	-	-	-	-	83.22	1.74	2.72

a_i represents the positions in the crack path where the parameters were evaluated. The analyses for every *DCB*-specimen were carried out for similar *y*-coordinates as indicated in Table 6.11. The *x*-coordinates correspond to the positions on the crack path, obtained from experimental results at the defined *y*-coordinates.

Table 6.11. Definition of the y-coordinate for the a_i positions

	a_3	a_5	a_7	a_9	a_{11}	a_{13}	a_{14}
y [mm]	*62*	*61 or 63*	*58 or 66*	*54 or 70*	*49 or 75*	*35 or 84*	*27 or 97*

y = 62 mm corresponds to the centre of the specimen

In the cyclic loaded specimens neither the stress intensity factor nor σ_T reached critical values before the position of the crack tip was at *15* mm from an edge.

On the example, Table 6.10, the *LEFM* is no longer applicable at the location a_9 because of the plastification of the ligament ($L_{rp}>1$). This was related to the decrease of the level of constrain at the surface-edge. This corner side effect is described in detail in reference [16]. Furthermore based on the results of the simulation, complete failure took place at the location a_{13}.

A summary on the predicted limit of *LEFM* applicability and plastic collapse are described in Table 6.12 for all *DCB*-notch configurations and loads.

Table 6.12. Plastic Collapse and complete failure positions

	Cyclic loading								***Quasi-static***							
	L-T				***T-L***				***L-T***				***T-L***			
	L_{rv}		***PC***		L_{rv}		***PC***		L_{rv}		***PC***		L_{rv}		***PC***	
	Δx	***y***	***Δx***	***y***	***Δx***	***y***	***Δx***	***y***	***Δx***	***y***	***Δx***	***y***	***Δx***	***y***	***Δx***	***y***
40 mm	20	104	20	104	34	90	34	90	54	70	54	70	57	67	57	67
90 mm	15	109	15	109	15	109	15	109	34	90	41	83	34	90	34	90
140 mm	N/A		N/A		N/A		N/A		49	75	33	91	58	74	33	91

**y = 62* mm *corresponds to the centre of the specimen; Δx = 0* mm *corresponds to the end of the notch*

From now on crack path predictions were only made up to $\sigma_T \geq R_m$, $K_v \geq K_{Ic}$ or the rest of the ligament shown $L_{rp} \geq 1.0$.

6.6 Crack path predictions

New *2D* crack path analyses, similar to those described in section 6.1.2, were performed taking into account all the results obtained in the previous sections, i.e. modelling a notch thickness, with the boundary conditions obtained in section 6.4 and taking into account K_v, σ_T, L_{rv} and L_{rp}.

First predictions were done by means of the *40* mm notched specimen. The number of elements increased during the crack propagation from 90 until 300.

For every model a traction force was applied in form of a bearing stress at the lower hole of the specimen. This force varies from *4* to *10* kN according to the results obtained in sections 6.1.1 and 6.3.2.

The crack propagation and turning predictions were performed by computing the fracture mechanics parameters and calculating the turning angle by means of different criteria, these were:

a) the Erdogan & Sih criterion (*E&Sih*) [62],

b) the Maximum Hoop Stress criterion (*MHS*) [3, 79],

c) the Pook criterion [104, 105],

d) the Cotterell & Rice criterion [63],

e) the Finnie & Saith, Kosai, Kobayashi & Ramulu and Shimamoto et al. criterion, called the *WEF*-criterion, with $r_c = 1.5$ mm [4, 62, 65, 66],

f) the Richard criterion with $A = -140^o$ and $B = -70^o$ [22],

g) the Shih criterion [30],

h) the Schöllmann criterion [22],

i) the Strain Energy Density criterion (*SED*) [73], and

j) the Maximal Principal Stress (*MPS*) criterion [96].

After each computation, the model was modified with a crack extension of *5* mm on the resulting direction. This iterative process was carried out until plastic collapse took place or the crack tip reached a side of the specimen.

Figure 6.46 illustrates the obtained crack path predicted by means of the procedure, criteria and models described above.

As observed in Figure 6.46 all criteria delivered similar crack path predictions. Furthermore, it was observed during the iteration process, that K_{II} can frequently drive the crack along a trajectory that is not necessarily the most energetically favourable, when taking into account purely global considerations. In other words, cracks did not follow $K_{II} = 0$ but deviate from the direction where K_{II} was *0*.

Although these results would be satisfactory for the crack path obtained during experimental test for the L-T specimen with a notch length of *40* mm charged under quasi-static load, the same path would be obtained for T-L specimens and even the same for the *DCB*-specimens charged under cyclic loading in both directions.

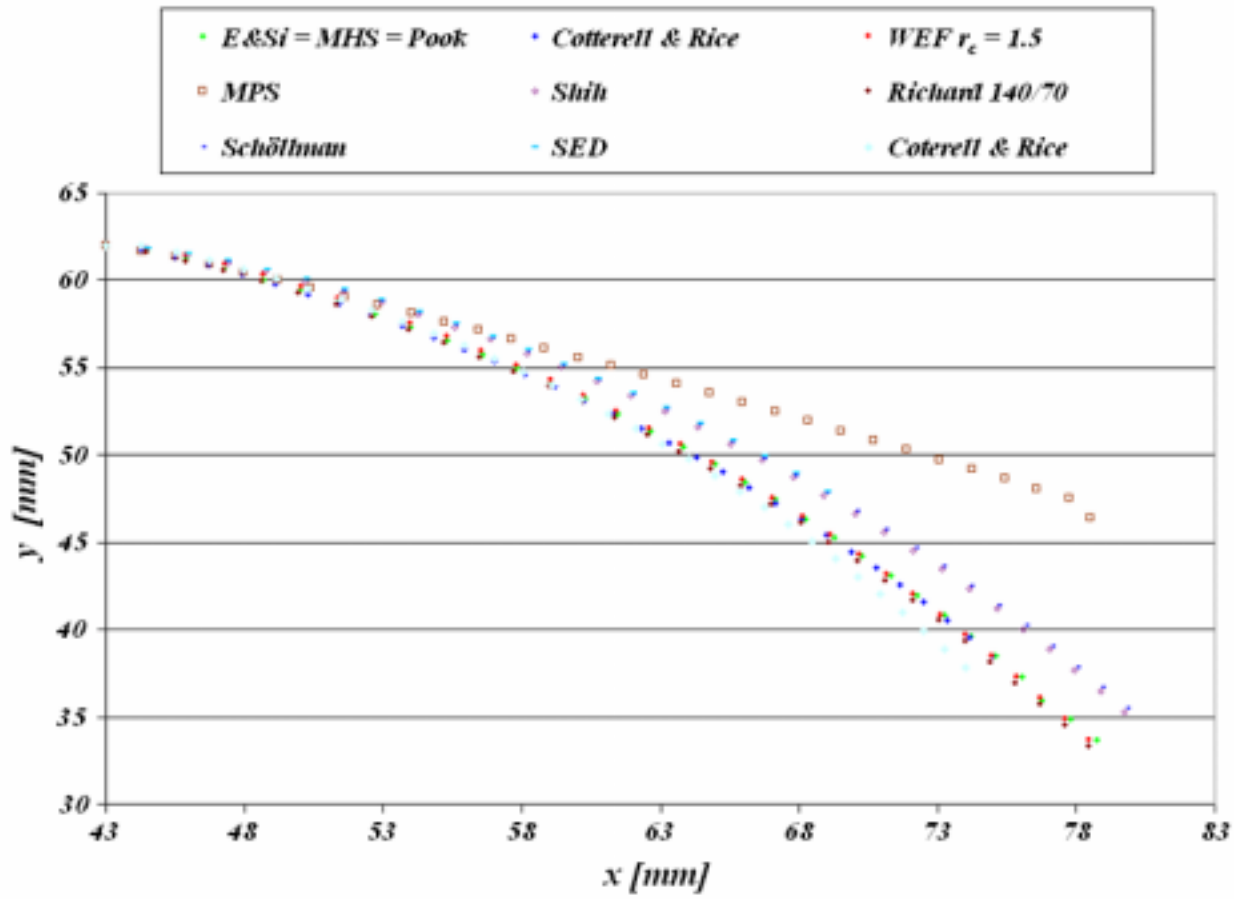

Figure 6.46. Crack path prediction by means of different crack turning criteria for the 40 mm notched DCB-specimen

Literature data and the analysis of experimental results indicate that there is a need to develop a concept able to take into account the type of loading and the anisotropy of the material simultaneously while using *LEFM*. This could be achieved by means of a parameter, which only defines the start of turning. After growth in this direction the specimen would be no longer symmetric and its future path should be more predictable, since the nominal asymmetry is then larger compared to random perturbations.

As discussed in chapter 2.4.2 there is a criterion, which takes into account the anisotropy of the material. This is the Buczek & Herakovich [71] and Boone et al. [72] criterion, in this work presented as the *WEFO*-criterion.

The results obtained by means of this last criterion are represented in Figure 6.47 for the 40 mm notched *DCB*-specimen. Although a different behaviour on the set point for the crack to turn was

obtained when simulating the crack propagating on T-L or T-L directions, the predicted crack paths were different than the test results.

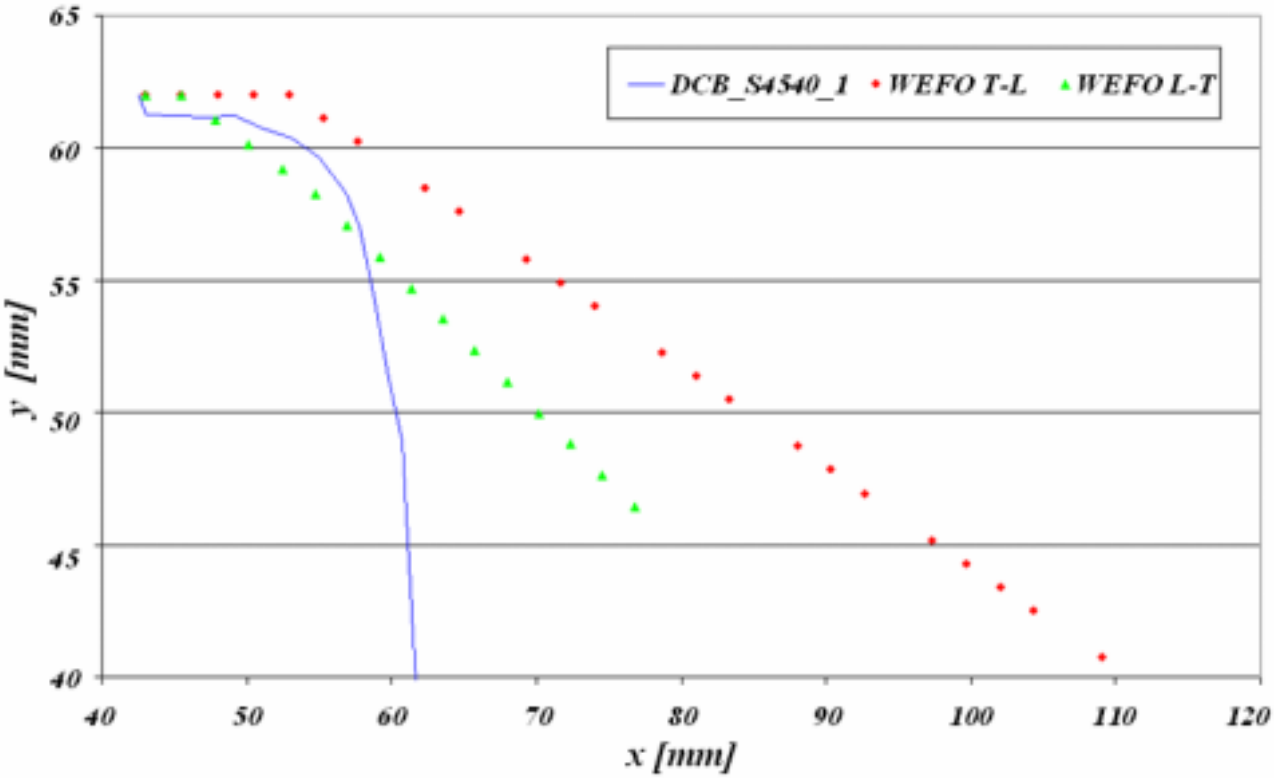

Figure 6.47. Crack path prediction using the WEFO-criterion on L-T and T-L direction

Based on the obtained results, the principal challenge for the correct simulation of these different paths consists on the definition of the initial point of turning. For the second order criteria this point is defined when the *T*-stress is positive and $r_c > r_0$. However, it is sometimes found in literature that cracks are directionally stable even when the *T*-stress is negative [79]. In order to explain this contradiction, the following possible hypotheses have been discussed by Pook [16].

a) A negative *T*-stress is a necessary but not sufficient criterion, so it does not guarantee instability.

b) There is an influence of the specimen boundaries [106].

c) There is an influence due to the presence of the crack tip plastic zone [107, 108].

d) The negative *T*-stress criteria are based on an infinitesimal analysis, so it is irrelevant to physical situations.

e) The size of the deviation used in assessing stability should be related to the length of the crack [109].

The most convincing explanations are those of Melin [109] and Pook [16], i.e. the presence of a crack tip plastic zone in conjunction with an infinitesimal analysis, even though the plastic zone is small enough which validates the use of the *SIF*.

In order to overcome the discrepancies, and to obtain a satisfactory parameter without ambiguities, to measure the crack path stability, the parameter needs to meet two necessary conditions. First, it must be non-dimensional and second, it must only include parameters describing the conditions at the crack tip [16].

Different parameters were proposed to overcome the incongruities generated by the use of *T*-stress criteria. These are:

a) The biaxial parameter, *B*, already introduced in section 6.4. However, *B* does not meet the second requirement, because the crack length, *a*, is used as a characteristic dimension. Furthermore, it was proved in reference [110] that the stiffness ratio between the frame and the specimen can have a significant impact on the results for *B*. Due to these reasons the *B*-parameter was discarded.

b) The ratio of the *T*-stress to the yield strength of the material, $R_{p0.2}$. This was proposed in reference [33] based on the observations that the *T*-stress affects directly the hydrostatic stress and the plastic constraints at the crack tip.

$$\tau = T/R_{p0.2} \quad (6.4.4)$$

c) The ratio of the *T*-stress to σ_x at some characteristic value of *r*, r_{ch}, on the crack line ahead of the crack. This is defined as T_R and σ_x is the direct stress parallel to the crack near the crack tip due to *Mode I SIF*, i.e. $\sigma_x = K_I/(2\pi r)^{0.5}$. This is an alternative approach proposed by

Pook [16] based on the biaxiality parameter. r_{ch} may be regarded as a crack tip parameter, which meets the second condition.

Due to the relation between the T_R and the *B*-parameter and because the biaxiality parameter is widely used in the literature, the T_R parameter was selected to substitute the role of the *T*-stress on the *WEFO*-criterion.

Analyses performed on biaxial loaded square sheets show that a crack path is stable for $B << 0.652$ and $T_R \leq 0.0216$ and unstable for $B \geq 0.786$ and $T_R \geq 0.0225$. The results indicate that the critical value of T_R, T_{Rc}, at which a cyclic loaded crack path becomes unstable is about *0.022*. For compact tension specimen the limit value was also found to be about *0.021*. For three point bend specimens with single edge notch, T_{Rc} was smaller than *0.021* and for doubler cantilever beam specimens T_{Rc} was slightly higher than *0.021* after [16].

6.7 Compilation of criteria and definitions

Aluminum wrought metal products, among others, are virtually isotropic elastically, but have a preferred direction of crack propagation resulting from the manner in which the material is processed. Furthermore, their processing has a symmetric character, e.g. rolled sheet or plate, and a two dimensional relation describing the crack growth resistance as a function of orientation will have two axes of symmetry.

Based on this last statement, literature review and part of work performed, the *WEFO*-criterion was modified including already defined parameters adapted for orthotropic behaviour in the two axes of symmetry.

a) According to Buczek & Herakovich [71] the crack path in anisotropic materials is supposed to follow the maximum of the ratio of the tangential stress to the crack growth resistance as showed in equation 2.4.12.

$$\overline{T} = \frac{\sin\varphi_c + \frac{K_{II}}{K_I}\left(3\cos\varphi_c - 1\right) - 2\Psi_I\left[\frac{K_{II}}{K_I}\sin\varphi_c - \frac{1}{3}\left(1+\cos\varphi_c\right)\right]}{\sin\left(\frac{\varphi_c}{2}\right)\left(2\cos\varphi_c - \Psi_I\sin\varphi_c\right)}$$

b) For some experiences some authors do not agree with the use of *T*-stress as the single parameter to determine the stability of the crack, even though the *T*-stress is positive [16, 65, 106-109]. Therefore, the parameter proposed by Pook [16] was used, i.e. T_R at some characteristic value r_{ch}.

$$T_R = 0.01\frac{T}{K_I} \quad (6.6.1)$$

c) Furthermore in order to take into account the effect of quasi-static loading or cyclic loading, the distance where the crack turning angle is evaluated, r_c, was defined as r_{cf} after [23] in equation 2.4.6.

$$r_{cf} = r_c\left(\frac{K_{\max}}{K_c}\right)^2$$

with K_{max} being the maximum equivalent *SIF* defined as:

$$K_{\max} = \sqrt{K_{I_{\max}}^2 + K_{II_{\max}}^2} \quad (6.6.2)$$

d) According to [23] even a perfectly unperturbed propagating crack must turn as σ_T approaches R_m. Thus, the ratio K_c/R_m was considered as a first approximation of the critical ratio of K_I/T at which crack turning must occur for unperturbed cracks according to Finnie & Saith [66]. The definition of r_c was then preferred to that given in equation 2.4.8.

$$r_c = \frac{9}{128\pi}\left(\frac{K_c}{\mathrm{R_m}}\right)^2$$

e) In the same way that K_c is dependent on the angle between the crack and the rolling direction, R_m and T_R are also dependent on it, as deducted from the experimental results. Therefore, both R_m and T_R were defined as elliptical functions, this is illustrated in Figure 6.48.

Based on the same assumptions as Buczek & Herakovich [71], the following expressions were proposed for $\xi = K_c$, R_m and T_R.

$$\bar{\xi}(\varphi) = \frac{1}{\sqrt{\cos^2\varphi + \bar{\xi}_m^{-2}\sin^2\varphi}} \quad (6.6.3)$$

$$\bar{\xi}(\varphi) = \frac{\xi(\varphi)}{\xi(0^o)} \quad (6.6.4)$$

$$\bar{\xi}_m(\varphi) = \frac{\xi(90^o)}{\xi(0^o)} = \frac{\xi_{L-T}}{\xi_{T-L}} \quad (6.6.5)$$

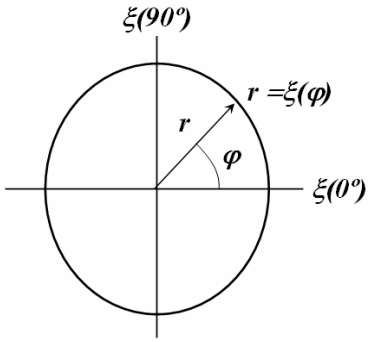

Figure 6.48. Schematic orthotropic parameter dependence (ξ)

f) On the non-linear analyses, it was observed that the fracture mechanics parameters, specially the *T*-stress, were highly sensitive to the increasing global plastification of the specimen. Therefore, it was assumed that the transition between stable and unstable crack propagation direction would be different for the specimens charged under quasi-static loading than for the specimens charged under cyclic loading.

By means of this criterion, crack paths were predicted for initial notches of *40* and *90* mm by means of different T_{Rc} values. The model with *40* mm was used to obtain in an iterative way the values of T_{Rc} for $\varphi = 0^o$ and for $\varphi = 90^o$ under static loading, and the *90* mm model was used to determine the critical value of T_R for cyclic loading. The results are summarised in Table 6.13.

Table 6.13. T_{Rc}-values for quasi-static and cyclic loading for both L-T and T-L directions

	Quasi-static load	***Cyclic load***
T_{Rc} (0º) i.e. T-L	0.029	0.034
T_{Rc} (90º) i.e. L-T	0.016	0.025

The crack paths for the *40* mm specimen under cyclic loading and the *90* mm and *140* mm specimen under quasi-static loading were predicted by means of the T_{Rc} values in Table 6.13. The same values were used to predict the crack path for the *CFS*-specimen using the model and the conditions illustrated in Figure 6.28.

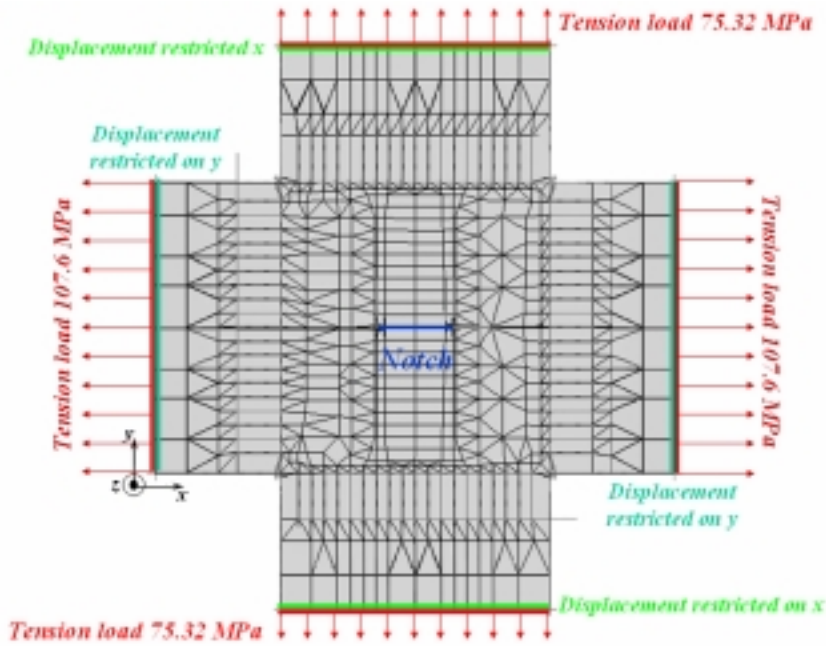

The predicted results are plotted in Figures 6.49 to 6.58 together with the experimental crack paths and plastic collapse.

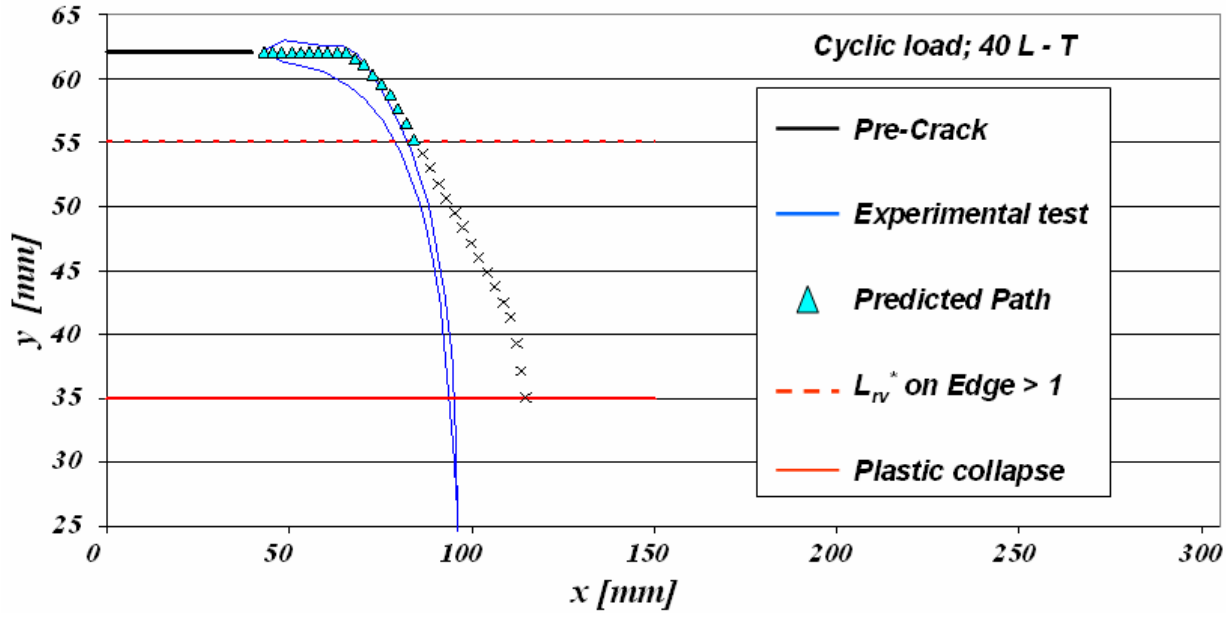

Figure 6.49. DCB-crack path prediction using the proposed criterion for the 40 mm pre-notched specimen in L-T direction under cyclic loading

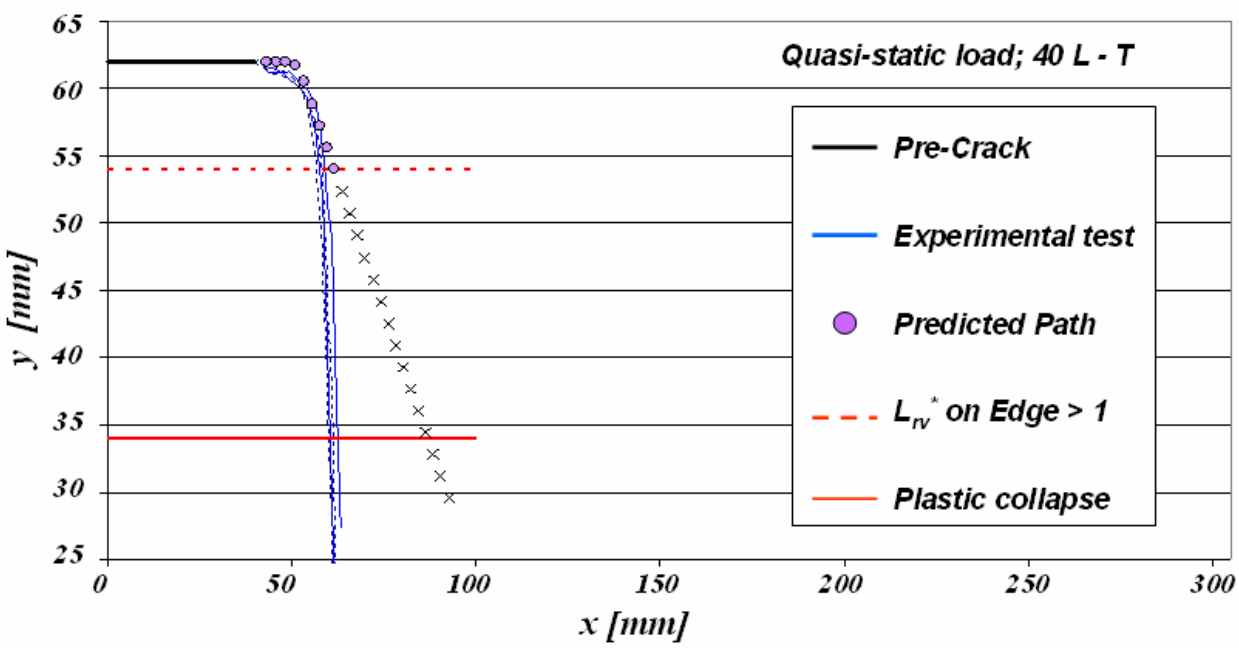

Figure 6.50. DCB-crack path prediction using the proposed criterion for the 40 mm pre-notched specimen in L-T direction under quasi-static loading

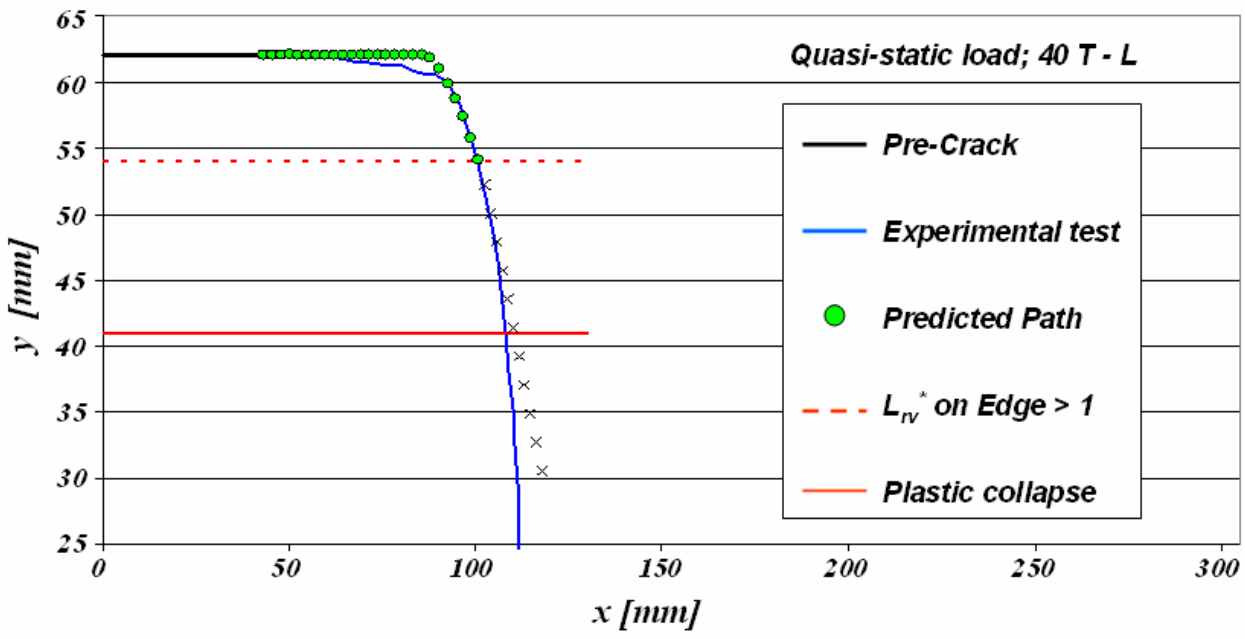

Figure 6.51. DCB-crack path prediction using the proposed criterion for the 40 mm pre-notched specimen in T-L direction under quasi-static loading

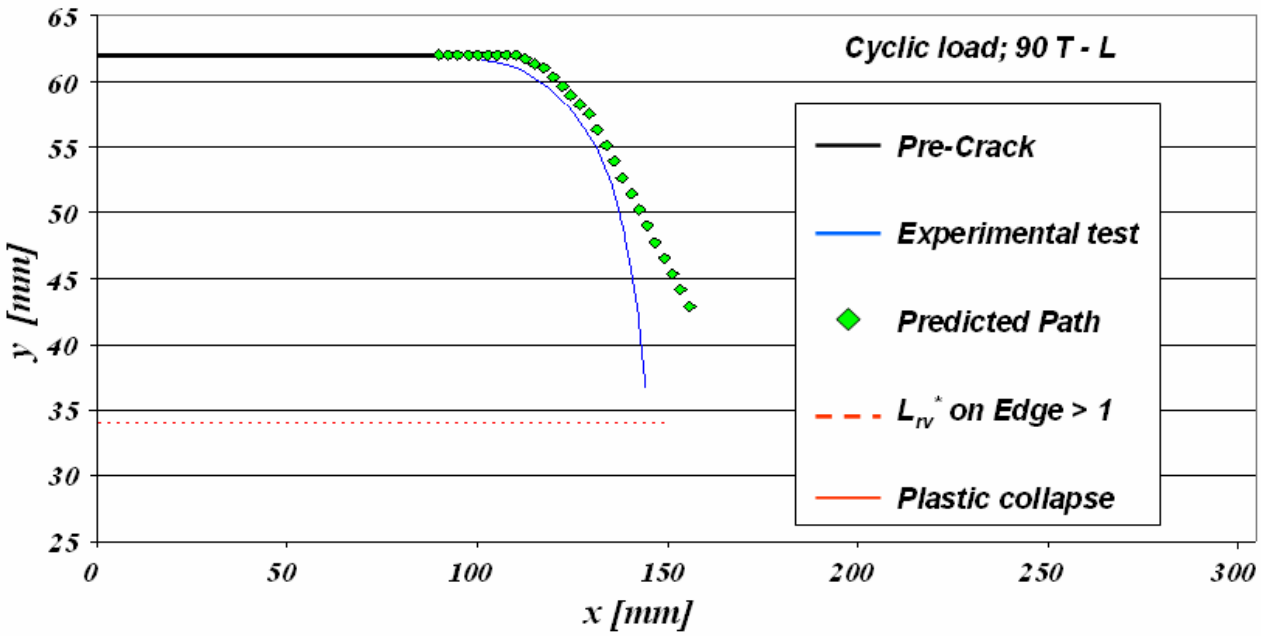

Figure 6.52. DCB-crack path prediction using the proposed criterion for the 90 mm pre-notched crack specimen in T-L direction under cyclic loading

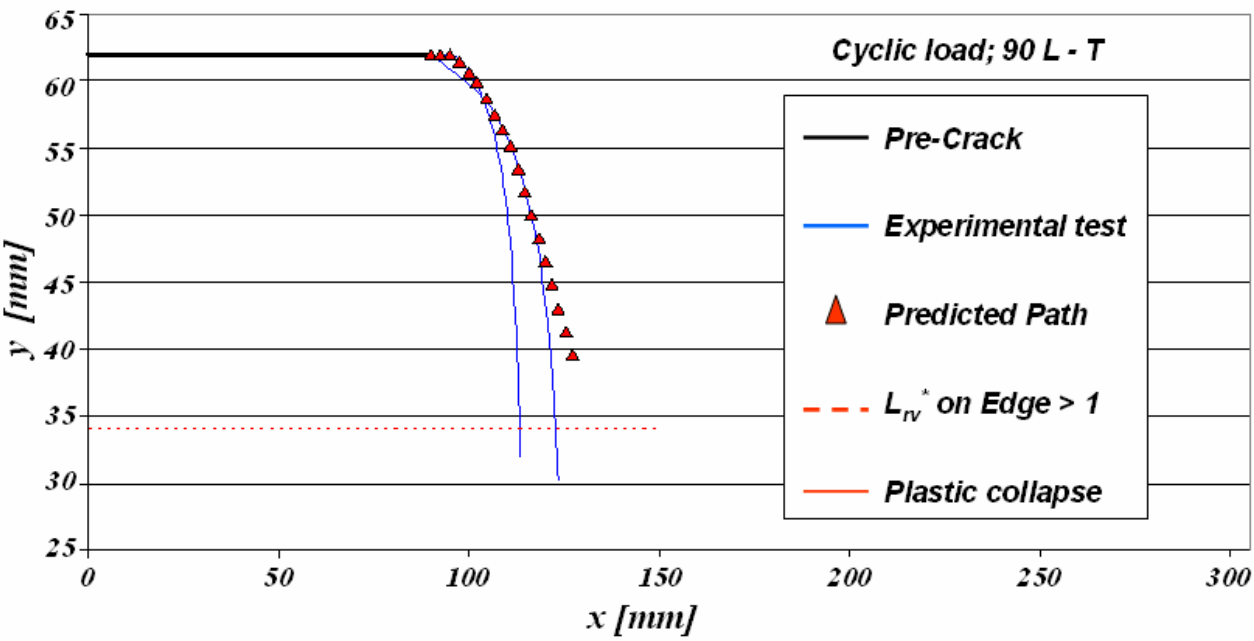

Figure 6.53. DCB-crack path prediction using the proposed criterion for the 90 mm pre-notched specimen in L-T direction under cyclic loading

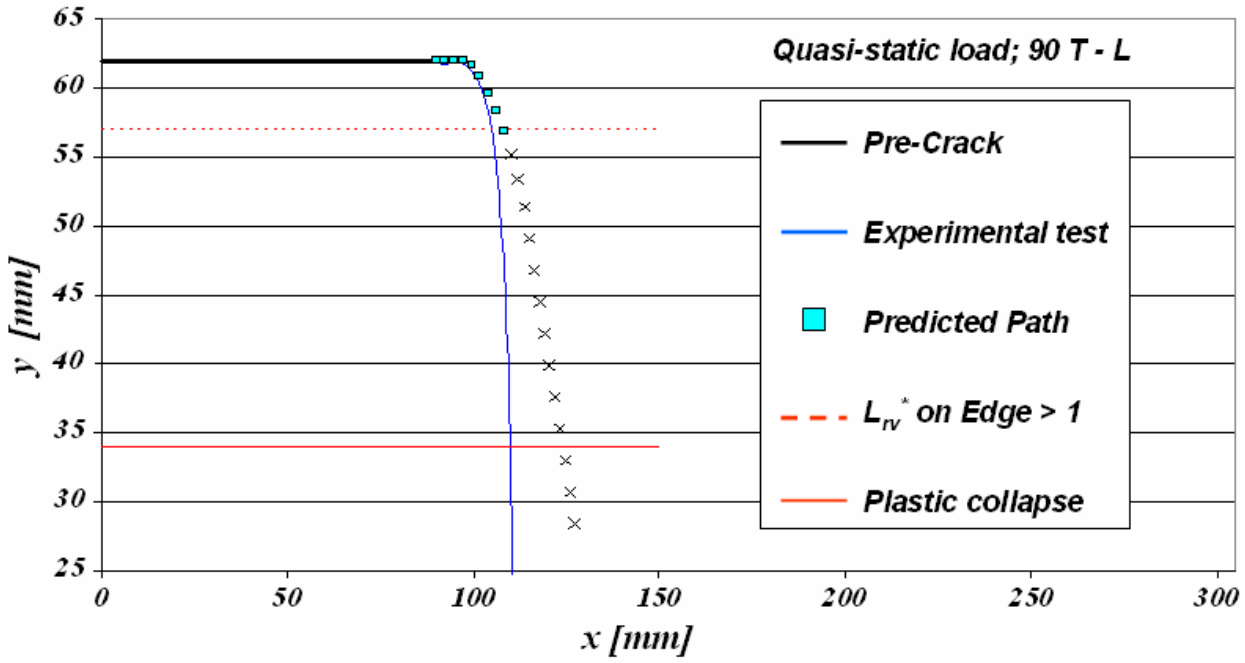

Figure 6.54. DCB-crack path prediction using the proposed criterion for the 90 mm pre-notched specimen in T-L direction under quasi-static loading

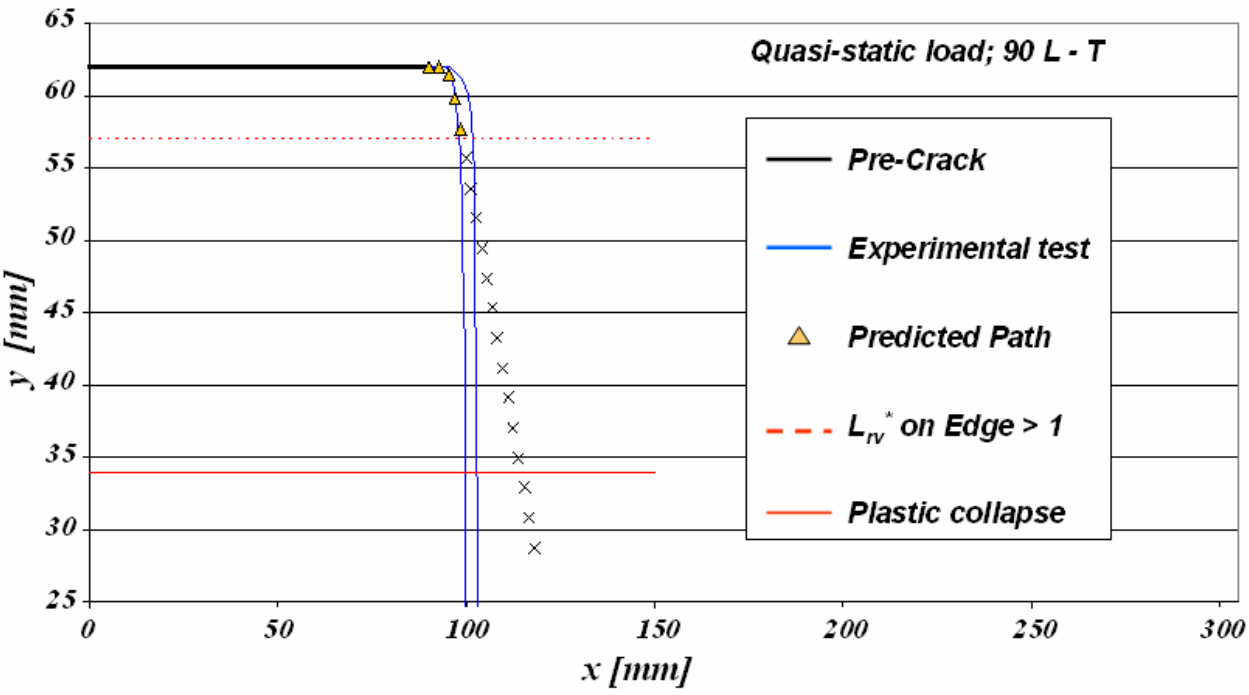

Figure 6.55. DCB-crack path prediction using the proposed criterion for the 90 mm pre-notched specimen in L-T direction under quasi-static loading

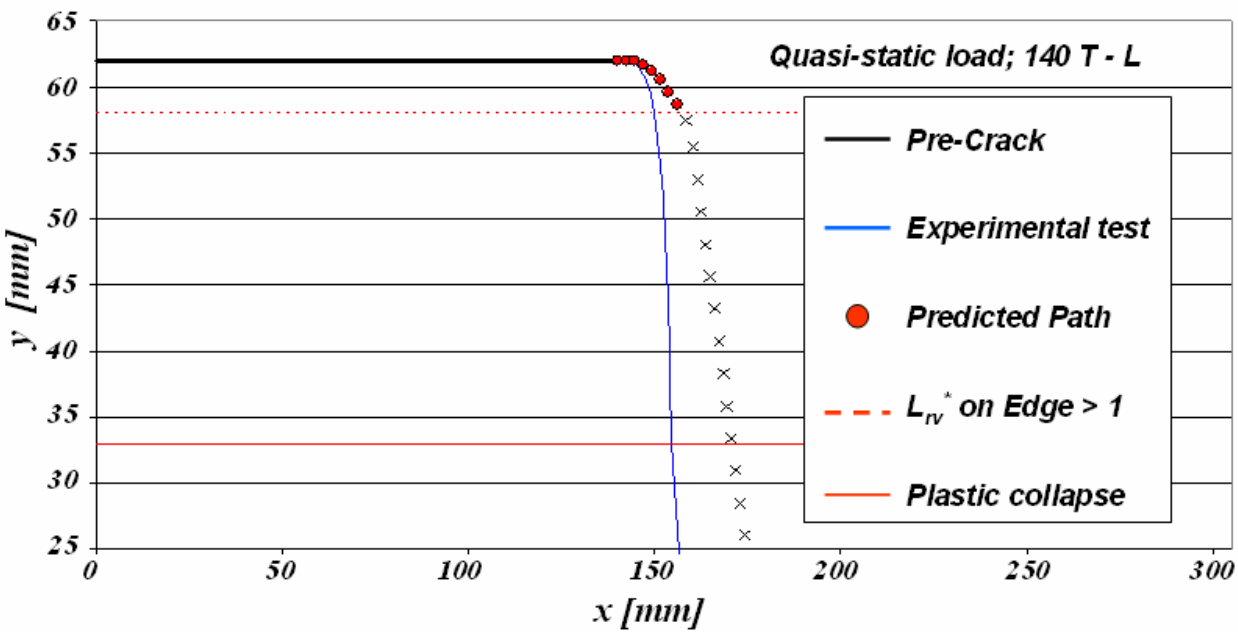

Figure 6.56. DCB-crack path prediction using the proposed criterion for the 140 mm pre-notched specimen in T-L direction under quasi-static loading

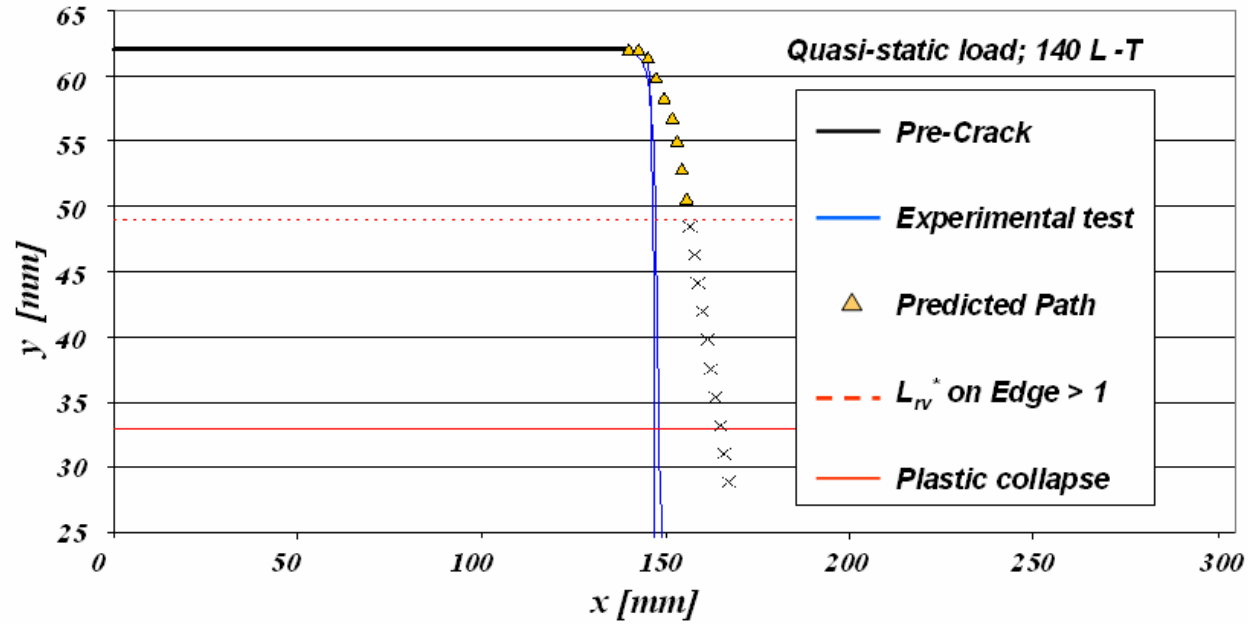

Figure 6.57. DCB-crack path prediction using the proposed criterion for the 140 mm pre-notched specimen in L-T direction under quasi-static loading

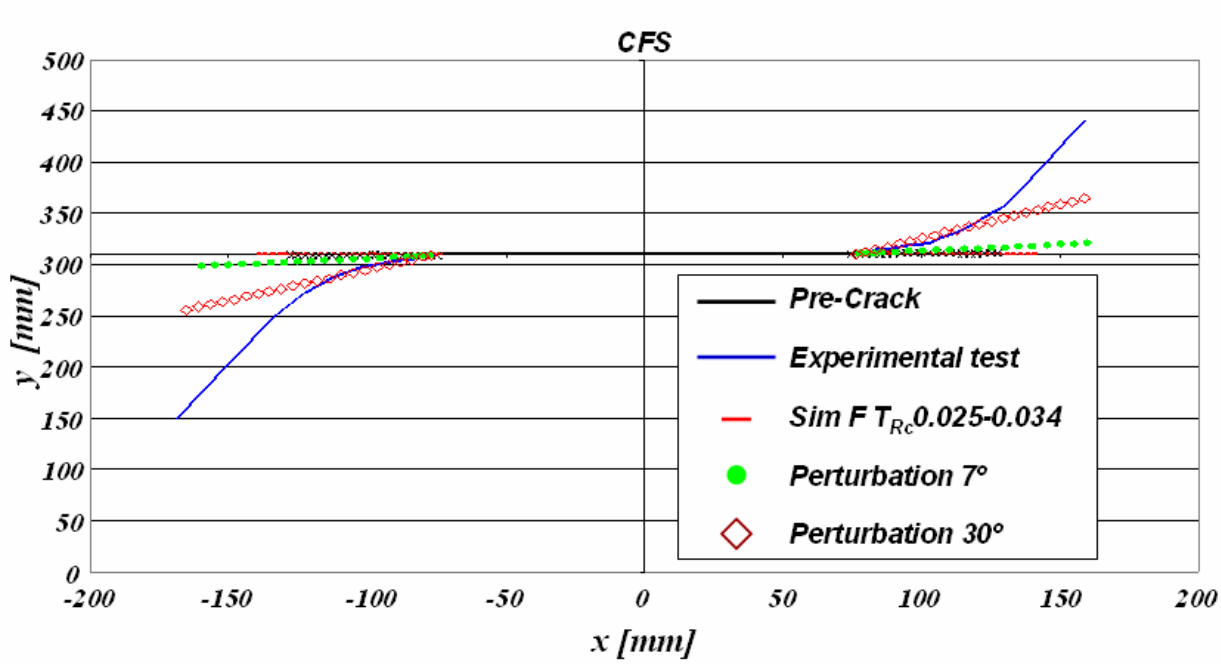

Figure 6.58. Crack path prediction using the proposed criterion on the CFS-specimen in L-T direction under cyclic loading

As observed in the figures above, the predicted crack path by means of the proposed criterion and the proposed model delivered satisfactory results on the *DCB*-specimens. The criterion differentiated crack propagation for L-T and T-L directions as well as cyclic and quasi-static load conditions.

But the *CFS*-predictions were not as satisfactory. This was related to the fact that the boundary conditions on the test could not be directly analysed. Besides this, only one specimen was tested. Furthermore, the alignment of the loads applied on the four arms of the specimen is a very difficult task and normally there is a deviation of some degrees. Another possible influence to the crack path, in the tested *CFS*-specimen, was the initiation of cracks on the grooves of the arms which propagated simultaneously with the notch crack during testing. This phenomenon was not studied in this work due to the lower number of tested specimens and the information available.

The results on the *CFS*-specimens show that the prediction of the path is very sensitive to crack perturbations, i.e. different crack paths are predicted from perturbations at the crack tip, for example due to inclusions or boundary grains.

It should be noted that crack path simulation on the *CFS*-specimen by means of the existent criteria predicted no turning, even with crack tip perturbations. Thus, comparing these predictions with those simulated by means of the proposed criterion, it can be concluded that the proposed criterion has more potential to deliver a better prediction than the existing criteria.